Thesis for the Degree of Licentiate in Engineering

Beyond Breakaway Corrosion:

Secondary Corrosion Protection of Iron-based Alloys

AMANDA PERSDOTTER

CHALMERS
UNIVERSITY OF TECHNOLOGY

Department of Chemistry and Chemical Engineering
Chalmers University of Technology
Gothenburg, Sweden 2020

Beyond Breakaway Corrosion: Secondary Corrosion Protection of Iron-based Alloys
AMANDA PERSDOTTER

Supervisor: Dr. Torbjörn Jonsson
Co-supervisor: Associate Professor Jesper Liske
Co-supervisor: Professor Jan-Erik Svensson
Examiner: Professor Lars-Gunnar Johansson

Thesis for the Degree of Licentiate in Engineering
No: 2020:06
Department of Chemistry and Chemical Engineering
Division of Energy and Materials
Unit of Environmental Inorganic Chemistry
Chalmers University of Technology
SE-412 96 Gothenburg
Sweden Telephone +46 31 772 1000

Cover: *Top left*: BSE-image showing a typical oxide microstructure of the secondary corrosion protection observed on iron-based alloys at intermediately high temperatures; *Bottom left*: BSE-image showing the oxide grains of the outward- and inward-growing scale formed on an Fe2.25Cr model alloy exposed for 48 hours to 5% O_2 + 95% N_2 at 600 °C, in the presence of K_2CO_3(s); *Right*: iSE-image of a cracked and delaminated oxide scale formed on Fe2.25Cr1Mo steel exposed for 24 hours to 5% O_2 + 20% H_2O + 75% N_2 at 400 °C in the presence of KCl(s).

Printed by [Chalmers Reproservice]
Gothenburg, Sweden 2020

Abstract

Metallic materials intended for high temperature applications must resist both mechanical and environmental degradation. The ability to withstand corrosion is an important aspect of high temperature materials and is of major concern in, for example, heat and power production. Nevertheless, corrosion is often a limiting factor in the lifetime of boiler components and it reduces the electrical efficiency and hinders the development of more economical and environmentally sustainable processes. The challenge of high temperature corrosion is often addressed by the use of high-alloyed steels, such as stainless steels and FeCrAl alloys. The corrosion resistance of stainless steels and FeCrAl alloys rely on the formation of a slow-growing, chromium- and/or aluminium-rich, corundum type oxide. However, in harsh corrosive environments these oxides are known to break down (i.e. 'breakaway corrosion') and a less protective, multi-layered, Fe-rich oxide is formed. One such example is in biomass- and waste-fired boilers, where the combustion process produces a corrosive environment, often resulting in breakaway corrosion in an early stage of operation. Thus, the corrosion propagation and lifetime of many key parts of the boilers, depend on the oxide scale formed after breakaway. This oxide scale is often considered non-protective and studies on the oxidation mechanisms controlling the corrosion propagation after breakaway are scarce.

In order to address, and systematically investigate the corrosion behaviour after breakaway, this thesis introduces the concept of primary and secondary corrosion protection for the oxide scales formed before and after breakaway, respectively. The concept is considered to be important for the development and selection of materials to be used in applications where the breakaway event cannot be prevented, e.g. in biomass- and waste-fired boilers, as well as for the development of lifetime predictive modelling tools for corrosion. A systematic study of the secondary corrosion regime is performed by well-controlled breakdown of the primary corrosion protection of Fe-based model alloys. The resulting oxide scales are subjected to detailed microstructural investigation to study the general aspects of the secondary corrosion protection and how its properties and microstructure changes e.g. by altered alloy composition.

The results show that the oxide scales formed after breakaway exhibit similar microstructural features on all the exposed FeCr(Ni/Al) model alloys and that the growth of the secondary corrosion protection is mainly diffusion-controlled. Thus, lifetime predictive tools using diffusion-based simulations, such as DICTRA, could be developed to predict corrosion both before and after breakaway. However, it is also shown that corrosive species (e.g. KCl) may affect the mechanical integrity of the oxide scale, resulting in growth processes that requires other types of models. Furthermore, the results show that the growth rate in the secondary corrosion regime may be influenced by the alloy composition, for example by adding Ni or a combination of Al/Cr. This behaviour is not directly connected to how well the primary corrosion protection withstands the exposure environment (i.e. the incubation time to breakaway). Thus, these findings indicate that research on the secondary corrosion protection has a large potential to improve the selection and development of alloys for use in corrosive environments, such as biomass- and waste-fired boilers.

Keywords: High temperature corrosion, Breakaway oxidation, Fe-based alloys

List of publications

This thesis is based on the following papers:

Paper I
A. Persdotter, M. Sattari, E. Larsson, M. A. Olivas Ogaz, J. Liske, T. Jonsson, Oxidation of Fe-2.25Cr-1Mo in presence of KCl(s) at 400 °C - Crack formation and its influence on oxidation kinetics, Corrosion Science, Volume 163 (108234), February 2020. https://doi.org/10.1016/j.corsci.2019.108234

Paper II
A. Persdotter, J. Eklund, J. Liske, T. Jonsson, Beyond Breakaway Corrosion - Influence of Chromium, Nickel and Aluminium on Corrosion of Iron-based Alloys at 600 °C. Accepted in Corrosion Science.

Statement of authors' contributions

Paper I
I am the principal author of the paper and am responsible for all of the SEM/EDX and FIB operations, as well as the sample preparation (supervised by Dr. Mohammad Sattari), and the post-processing and analysis of the STEM results. The TEM was operated mainly by Dr. Mohammad Sattari and partly by me. Exposed samples and complementary mass gain data were provided by Dr. Erik Larsson and Dr. Mercedez Andrea Olivas Ogaz. The XRD analysis was performed under the supervision of Johan Eklund.

Paper II
I am the principal author of the paper and am responsible for the majority of the SEM/EDX results and FIB operation. Exposed samples and complementary TGA data for the analysis were provided by PhD student Johan Eklund and diploma worker William Fung, who also carried out the preparation and SEM/EDX analysis of some of the BIB milled samples. Some exposures and plan-view imaging of the primary corrosion protection were also performed by Dr. Mercedez Andrea Olivas Ogaz and PhD student Julien Phother Simon.

Related publications not included in this thesis:

J. Eklund, B. Jönsson, A. Persdotter, J. Liske, J.-E. Svensson, T. Jonsson, The influence of silicon on the corrosion properties of FeCrAl model alloys in oxidizing environments at 600 °C, Corrosion Science 144, 266–276 (2018). https://doi.org/10.1016/j.corsci.2018.09.004

M. A. Olivas-Ogaz, J. Eklund, A. Persdotter, M. Sattari, J. Liske, J. -E. Svensson, T. Jonsson, The Influence of Oxide-Scale Microstructure on KCl(s)-Induced Corrosion of Low-Alloyed Steel at 400 °C, Oxidation of Metals 91:291–310, (2019). https://doi.org/10.1007/s11085-018-9881-2

Larsson, E., Liske, J., Persdotter, A. et al. The Influence of KCl and HCl on the High-Temperature Oxidation of a Fe-2.25Cr-1Mo Steel at 400 °C. Oxidation of Metals 93, 29–52 (2020). https://doi.org/10.1007/s11085-019-09943-9

Acknowledgements

First of all, I would like to express my gratitude to everyone who made this thesis possible and who helped me during this work.

I would like to thank my supervisors Dr. Torbjörn Jonsson, Assoc. Prof. Jesper Liske and Prof. Jan-Erik Svensson for the great support and many interesting discussions.

Furthermore, I would like to thank my examiner Lars-Gunnar Johansson and acknowledge the High Temperature Corrosion Centre (HTC) and VINNOVA, Sweden's Innovation Agency, for funding, together with the Swedish Energy Agency and the member companies (AB Sandvik Materials Technology, Kanthal AB, Energiforsk AB, MH Engineering AB, Thermo-Cale Software AB, Valmet Technologies Oy, Sumitumo SHI FW Energia Oy, Babcock and Wilcox Volund A/S, and MEC BioHeat and Power A/S).

I am sincerely grateful to all the PhD students and diploma workers who have helped in providing samples and complementary data for the studies described in this thesis. Special thanks to PhD student, Johan Eklund, Dr. Mercedez Andrea Olivas Ogaz, Dr. Erik Larsson and William Fung.

I would also like to thank PhD student Johan Eklund and Dr. Mercedez Andrea Olivas Ogaz for all their support and inspiring discussions.

Last, but not least I would like to thank all my present and previous colleagues in the Unit of Environmental Inorganic Chemistry for providing a fun working environment as well as my family for all the love and support and for putting things in perspective.

Amanda Persdotter, Gothenburg, 05 2020

Contents

1

Introduction

High temperature corrosion represents a major challenge in many high temperature applications and results in increased material and maintenance costs. The challenge is often addressed by the use of high-alloyed steels, such as stainless steels at intermediately high temperatures (<900 °C) and FeCrAl alloys at higher temperatures (>900 °C). The corrosion resistance of stainless steels and FeCrAl alloys are well known to rely on the formation of a slow-growing, chromium (Cr)- and/or aluminium (Al)-rich, corundum type (M_2O_3) oxide scale formed in mildly corrosive environments [1–3].

However, the presence of corrosive species such as, e.g. water vapour and alkali may result in breakdown of the M_2O_3 oxide scales (i.e. 'breakaway corrosion') and the formation of a less protective, multi-layered, Fe-rich oxide scale (see e.g. [4–27]). This is the typical situation for e.g. superheaters in biomass- and waste-fired boilers, where breakaway corrosion is often observed in an early stage of operation [28–36]. Thus, the corrosion propagation in the superheaters must rely on the oxide scale formed after breakaway.

The oxide scales formed after breakaway have features similar to those of the Fe-rich scales formed on low-alloyed steels, being composed of an outward-growing iron oxide scale and a mixed inward-growing scale (see e.g. [4, 9, 10, 12, 25, 27, 37]). Thus, the corrosion properties of Fe-rich oxide scales are not only of interest with respect to classical iron oxide formers, such as low-alloyed steels, but also for other Fe-based alloys, such as stainless steels and FeCrAl alloys after breakaway corrosion. In applications where breakaway corrosion cannot be prevented, such as biomass- and waste-fired boilers, the protective properties of this Fe-rich oxide scale are of great concern. The properties of the scale formed on stainless steels and FeCrAl alloys after breakaway have not been extensively studied. However, recent studies [25, 37] have indicated that the oxide scale formed after breakaway may be improved by varying the amounts of different alloying elements. Thus, a better understanding of the oxidation properties of the oxide scale formed after breakaway could assist material developers in producing tailor-made materials with different types of corrosion resistance based on the expected application conditions. In addition, the development of lifetime predictive modelling tools for corrosion (see e.g. [38, 39]), requires appropriate input values as to which type of oxide scale should be modelled and which processes are rate-limiting for the growth of this oxide scale.

This thesis introduces the concept of primary- and secondary corrosion regimes for the

oxidation before and after breakdown of the slow-growing, Cr/Al-rich, M_2O_3 oxide scales formed on stainless steels and FeCrAl alloys in mild environments (i.e. the primary corrosion protection). The terminology is considered important for future material research and development, as well as for the choice of materials to be used in applications where breakaway corrosion cannot be prevented, e.g. in biomass- and waste-fired boilers.

The concept is implemented in this work by investigating how the oxide microstructure and oxidation properties of the multi-layered, Fe-rich oxide scale (i.e. the secondary corrosion protection) are affected by the variation in alloy composition, as compared to the primary corrosion protection, at an intermediately high temperature (600 °C). This is done by investigating the oxide scales formed, before and after breakdown of the primary corrosion protection, on a wide set of Fe-based model alloys containing varying concentrations of Cr, Ni and Al. The influences of different corrosive species on the secondary corrosion protection is also investigated briefly by studying the microstructural changes in the oxide formed on a low-alloyed steel exposed in different chlorine- and/or alkali-containing environments.

2

High temperature corrosion

High temperature corrosion can entail several processes such as oxidation, chlorination, alkaline corrosion, nitridation, metal dusting etc. This chapter focuses on oxidation and includes a short summary of oxidation theory and descriptions of the oxides that typically form on three important material classes used in high temperature applications: low-alloyed steels; stainless steels; and FeCrAl alloys. The focus of this work is on the oxidation properties of the oxide scales formed on these materials in mild and harsh corrosive environments (i.e. before and after 'breakaway corrosion'), in particular with regard to the Fe-rich oxide scales formed after breakaway.

2.1 Metal oxidation

Metal oxidation refers to the reaction of metals with oxygen according to Reaction 2.1:

$$\mathrm{aM(s)} + \frac{\mathrm{b}}{2}\mathrm{O_2(g)} \rightarrow \mathrm{M_aO_b(s)} \tag{2.1}$$

, where M represents the metal, O the oxygen, $\mathrm{M_aO_b}$ the metal oxide, and a and b are stoichiometric constants [1]. The metal oxides can be described as oxygen- and metal-containing sub-lattices with the chemical formula $\mathrm{M_aO_b}$. It should be noted that the chemical formula is stoichiometric which is not true for most metals. A more accurate formula for non-stoichiometric oxides would be $\mathrm{M_{a\pm x}O_{b\pm y}}$, wherein oxides with a metal excess as well as metal and oxygen deficiencies exist. However, for the sake of simplicity, in this work, all oxides are described with the stoichiometric formula.

2.1.1 Thermodynamics

In general, metals are thermodynamically unstable in the presence of oxygen and will spontaneously form oxides if the oxygen partial pressure, p_{O_2}, exceeds the dissociation pressure of that specific oxide [1]. This is represented by the Gibbs free energy, plotted as a function of e.g. p_{O_2}, in the Ellingham diagram shown in Figure 2.1. The Ellingham diagram can be used to compare the stabilities of oxides at different temperatures and p_{O_2} values, to predict which oxides that are expected to form at different p_{O_2} levels, e.g. at different depths of a growing oxide scale.

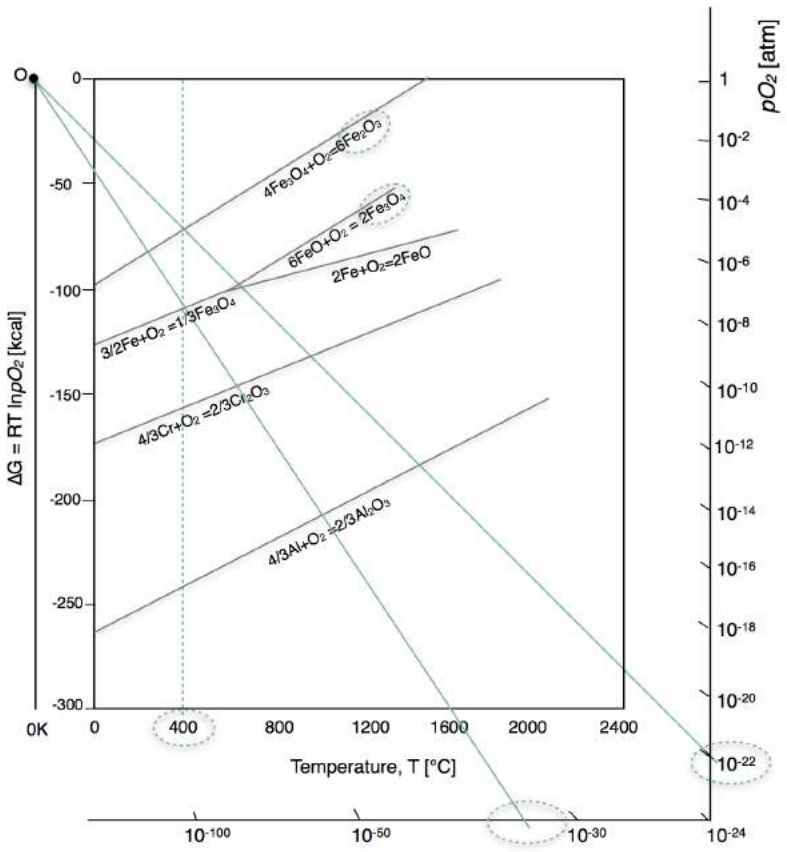

Figure 2.1: Ellingham diagram, reconstructed from data in [1], for a few selected oxides that are relevant to this work. The dissociation pressure (i.e. the lowest possible p_{O_2} level required for the oxide to form) can be determined graphically for the temperature and oxide of interest. A straight line is drawn from the 'O' point on the left margin, through the point at which a vertical temperature line crosses the free energy curve of the oxide of interest. The dissociation pressure is determined at the point where the straight line crosses the p_{O_2}-axis.

2.1.2 Oxide formation and growth

The oxidation process is initiated by the adsorption and reduction of oxygen anions at the metal surface, which then react with metal cations to form oxide nuclei that grow laterally to cover the entire metal surface. When the surface is completely covered the formed oxide scale will continue to increase in thickness as long as the reacting species are allowed to pass through the scale. The formed oxide scale may act as a protective barrier between the metal and the surrounding atmosphere, provided that the oxide scale is slow-growing, continuous, dense, intact, well-adherent, and inert to reactions such as evaporation and melting, thereby hindering migration of charged species, and consequently the oxide growth from proceeding [1]. Thus, the oxidation propagation, and the corrosion resistance, is determined by how efficiently this barrier obstructs the diffusion of charged species through the scale.

The charged species can move through the oxide through bulk diffusion or short-circuit diffusion. Bulk diffusion is determined by the defect structure of the oxide lattice, whereas

short-circuit diffusion occurs along microscopic defects, such as cracks, voids and grain boundaries [1,40] (see Figure 2.2). Thus, the defect structure and influences of microstructural changes of different oxides must be understood in order to make the barrier more efficient, so as to improve the corrosion protection of the formed oxide scale.

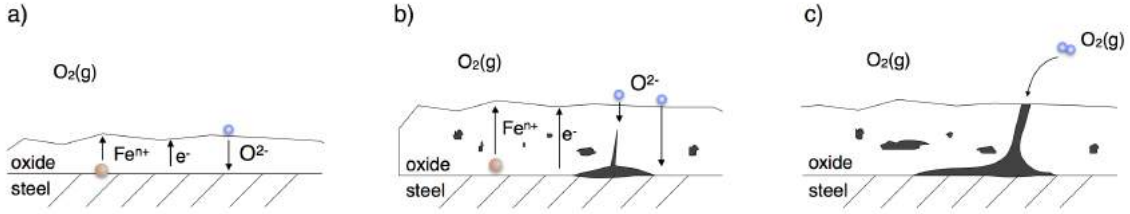

Figure 2.2: Schematic of the process of oxide scale growth through migration of reacting species through the oxide scale, as described by [1]. Migration through the scale occurs via: a) bulk diffusion, b) microstructural defects (e.g. micro-cracks, voids and grain boundaries); and c) macro-cracks and pores.

The oxide may grow by either outward diffusion of metal cations (outward-growing scale) or by inward diffusion of anions (inward-growing scale). The outward-growing scale is formed at the gas/scale interface while the inward-growing scale is formed at the scale/metal interface (see Figure 2.3b). Many oxide scales grow through both inward and outward diffusion, and the two different types of scales can be determined by marker experiments. In this work, the presence of Cr in the spinel oxide is used as an indirect marker to distinguish inward- and outward-growing spinel oxides. This is possible since the diffusion of Cr^{3+} (and Al^{3+}) in the spinel structure is known to be much slower than that of Fe^{2+} (see Figure 2.3a) [41, 42]. Therefore, as soon as the spinel has formed, the Cr ions will remain fixed, resulting in an outward-growing scale that is almost completely free of Cr.

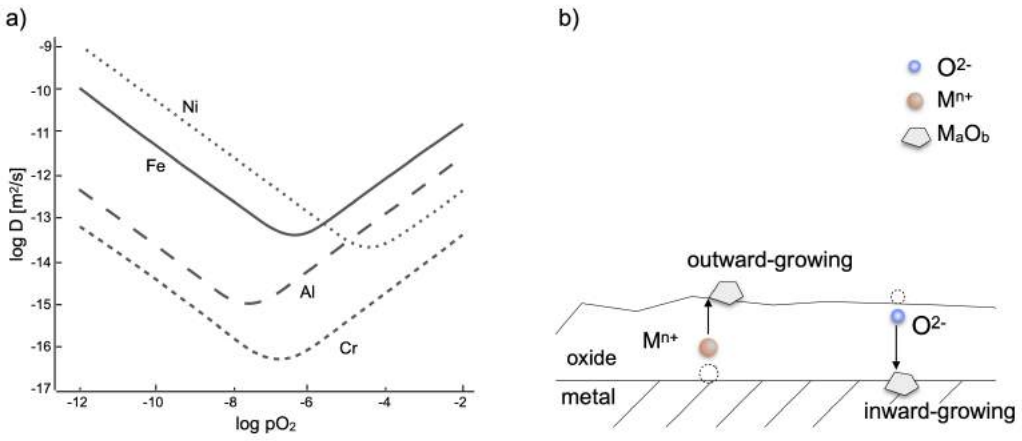

Figure 2.3: a) Diffusivities of cations (Fe, Cr, Al, Ni) in Fe_3O_4 at 1200 °C. Data for reconstructing the figure were reported by Dieckmann and Schmalzried [43] and summarised by Van Orman and Crispin [42]. b)

2.1.3 Oxidation kinetics

The rate of which the oxide scale grows, i.e. the oxidation kinetics, can be determined by recording mass changes at different exposure times. This can be done either by continuous thermogravimetric analysis or by several regular furnace exposures conducted for different durations. However, the recorded mass changes may also be influenced by other reactions that are not directly linked to the oxide scale growth. Therefore, measurement of oxide scale thickness is a more accurate (although more time-consuming) way to determine the growth rate of oxide scales.

The oxidation kinetics are often discussed in terms of ideal rate laws, as to understand the properties of the oxide scale [1] (see Figure 2.4). Oxide scales formed at high temperatures are commonly assumed to grow according to parabolic kinetics ($x^2 \propto t$, where x is the oxide thickness and t, time), which means that the growth is diffusion-controlled and limited by the transport of charged species through the scale, such that it slows down as the oxide scale grows thicker. The parabolic rate law was derived by Tammann in the 1920's [44] and refined by Wagner in 1933 [45]. Thus, parabolic kinetics is explained by that the oxide scale acts as a diffusion barrier. However, when the diffusion barrier is not sufficient, the growth kinetics may become more or less linear, being limited e.g. by the rate of reaction, instead of the diffusion of charged species (see Figure 2.4).

If a protective oxide scale loses its ability to act as a protective barrier, a transition from slow, parabolic kinetics to a more rapid (commonly assumed linear) kinetics is often observed, a process referred to as 'breakaway corrosion' (see Figure 2.4). The oxide scale formed after breakaway is considered non-protective and the breakaway event often results in rapid degradation and catastrophic failure of the material. However, in practice the scale formed after breakaway may also act as a diffusion barrier, with initial linear kinetics that levels off after a certain time. This work investigates the oxide scales formed both before and after breakaway to increase our understanding as to how to improve the corrosion protection also after breakaway.

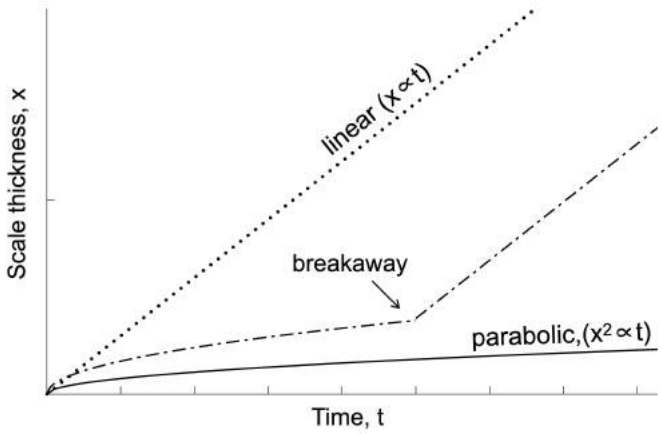

Figure 2.4: Schematic of the ideal rate laws for oxide scale growth at high temperatures: linear growth , parabolic growth, and breakaway oxidation.

2.2 Corrosion protection of Fe-based alloys

2.2.1 Stainless steels and FeCrAl alloys

Stainless steels and FeCrAl alloys exposed to mildly corrosive environments rely on the formation of a continuous, slow-growing, Cr- and/or Al-rich, corundum-type (M_2O_3) oxide scale [1–3]. Hematite (Fe_2O_3) is another corundum-type oxide that can form solid solutions with Cr_2O_3 (chromia) and Al_2O_3 (alumina) oxide scales, resulting in mixed M_2O_3 oxides, such as those formed on stainless steels ($(Cr_x,Fe_{1-x})_2O_3$)). The corundum type of crystal structure consists of a hexagonal sub-lattice of oxygen ions with trivalent cations (M^{3+}) positioned in two-thirds of the octahedral holes, as illustrated in Figure 2.5 [1].

Both the Cr- and Al-rich M_2O_3 oxides are comparatively stable at high temperatures (see Ellingham diagram in Figure 2.1), and are considered slow-growing oxides due to their low ion mobility and defect concentration [1]. Provided that the oxide scales are well-adherent and form continuously over the metal surface, the growth kinetics of both the Cr-rich and Al-rich M_2O_3 oxides are often slow and parabolic, typical for a diffusion-controlled growth process, as described in section 2.1.3.

Thus, the Cr-rich M_2O_3 oxide scale formed on stainless steels ($(Cr_x,Fe_{1-x})_2O_3$) exhibits excellent corrosion protection at intermediately high temperatures (<900 °C) while FeCrAl alloys are designed to provide an improved corrosion protection at higher temperatures (>900 °C). The designed corrosion protection of FeCrAl alloys involves the formation of α-Al_2O_3, which mainly exists at temperatures above 900 °C [1, 5, 46]. However, at lower temperatures (<900 °C) the corrosion protection may be attributed to transient aluminas or Cr-rich oxides, with properties similar to the oxide formed on stainless steels [1, 47].

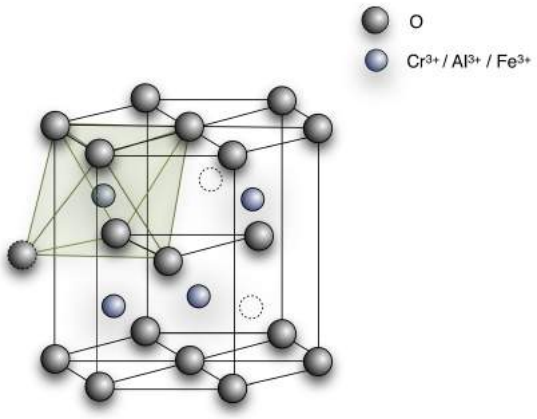

Figure 2.5: Illustration of the atomic distribution in the corundum crystal structures of chromia (Cr_2O_3), alumina (Al_2O_3) and hematite (Fe_2O_3) as described by [1].

2.2.2 Low-alloyed steels

Low-alloyed steels do not contain enough Cr to form a Cr-rich M_2O_3 oxide scale. As a consequence, the corrosion protection of low-alloyed steels is conferred by an Fe-rich oxide scale that is similar to the scale formed on pure iron. Corrosion of iron and low-alloyed steels have previously been studied extensively and are summarised e.g. by Chen and Yuen [48]. The oxide scales formed on iron and low-alloyed steels are multi-layered and consist of inward- and outward-growing Fe-rich oxides (see the example in Figure 2.6). The inward-growing scale is a spinel-type oxide [Fe_3O_4 for pure iron and $(Fe_{1-x-y},Cr_xM_y)_3O_4$, $x+y=1$ for low-alloyed steels] while the outward-growing oxide is composed of hematite (Fe_2O_3) on top of magnetite Fe_3O_4) (and wustite, $Fe_{1-x}O$, at temperatures >570 °C.

The layered structure (see Figure 2.6) can be explained by the thermodynamic stabilities of the different oxides and the chemical gradient of oxygen throughout the scale. Thus, the different oxides can be predicted by the Ellingham diagram (see Figure 2.1) if defects such as voids and cracks are not taken into account [1]. Thus, hematite forms in the top layer of the multi-layered oxide scale (high p_{O_2}) while magnetite (and mixed spinel) often forms below a layer of hematite (lower p_{O_2}), as can be seen in Figure 2.1.

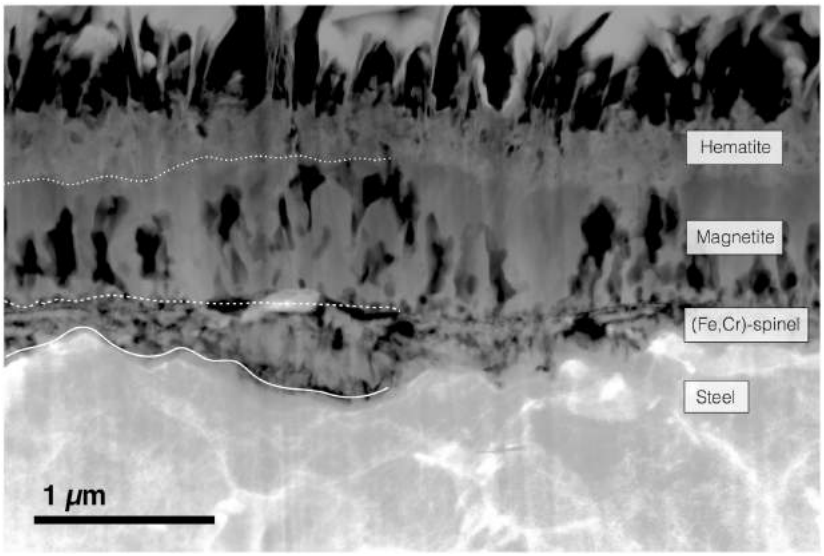

Figure 2.6: Characteristic microstructure of the multi-layered, Fe-rich oxide scale formed on a low-alloyed steel.

Hematite (Fe_2O_3) has a corundum-type crystal structure, similar to those of chromia and alumina, in which the oxygen anions are arranged in a hexagonal array with trivalent iron ions (Fe^{3+}) in two-thirds of the octahedral holes [49, 50] (see Figure 2.7).

Magnetite has an inverse spinel structure [$Fe^{3+}(Fe^{2+}Fe^{3+})O_4^{2-}$], illustrated in Figure 2.7, in which the oxygen anions form a face centre cubic (FCC) lattice and the metal cations are positioned in one-eighth of the tetrahedral (Fe^{3+}) holes and half of the octahedral holes (Fe^{2+} shared with Fe^{3+}) [1, 49].

The mixed inward-growing spinel, present at the scale/metal interface in Figure 2.6, has a similar crystal structure to magnetite, although with differences in the distributions of divalent and trivalent cations in the octahedral and tetrahedral holes (normal spinel) [1, 49, 50]. The structure of the mixed spinel ($M^{2+}M^{3+}M^{3+}O_4$) limits the amount of divalent and trivalent ions. While Fe^{2+} and Fe^{3+} are both present in, for example, magnetite, the oxidation states of Cr, Al and Ni are more restricted (Cr^{3+}, Al^{3+} and Ni^{2+}) [51]. Thus, the different alloying elements do not compete equally for all the sites in the spinel. Assuming the oxidation states mentioned above, the Fe^{3+}, Cr^{3+} and Al^{3+} all compete for the trivalent sites (maximum of 67.7 at%) while Fe^{2+} and Ni^{2+} compete for the divalent (maximum of 33.3 at%).

Wustite also forms on iron and low-alloyed steels at temperatures above 570 °C [49]. However, wustite is not thermodynamically stable at lower temperatures, and the presence of alloying elements such as Cr shifts the equilibrium conditions for this oxide scale to higher temperatures [52]. Thus, wustite is not expected to be observed in this work.

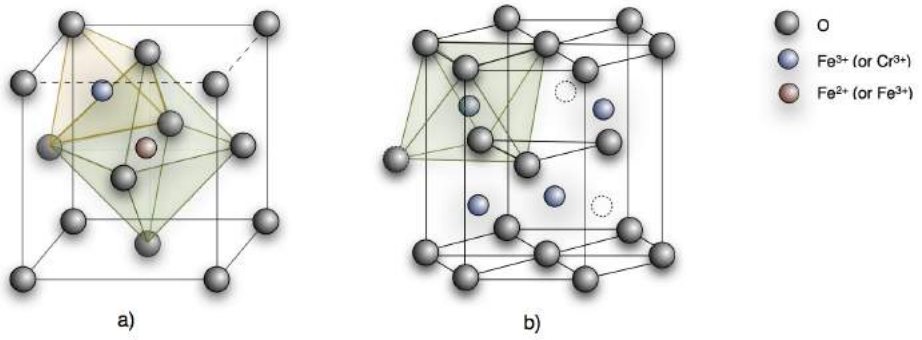

Figure 2.7: Illustration of the atomic distribution in the crystal structures of: a) hematite (corundum); and b) magnetite/spinel. For the mixed Fe,Cr,M-spinel, up to 67% of the Fe-sites could be replaced by, for example, Cr^{3+} (corresponding to $FeCr_2O_4$).

2.2.3 Breakdown mechanisms and corrosion after breakaway

The corrosion protection formed on stainless steels and FeCrAl alloys in mildly corrosive environments may, for several reasons, not be sustained in harsher corrosive environments (e.g. at higher temperatures [4, 22, 53]) or in the presence of water vapour [6–17, 23–25, 37, 54], alkali and/or chlorine containing species [18–21, 26, 27, 37, 55–59]. If this Cr/Al-rich M_2O_3-type of corrosion protection breaks down, the oxidation proceeds through the formation of a faster-growing, Fe-rich oxide, similar to those formed on low-alloyed steels and iron. This event is often referred to as breakaway corrosion. However, previous studies have indicated that the oxide scale formed after breakaway of stainless steels and FeCrAl alloys may act partly protective (see e.g. [25, 37]). Thus, in this work, the event of breakaway corrosion is not treated as a stage of failure, but rather as a transition from one type of corrosion regime, i.e. **primary corrosion protection** (before breakaway) to another, i.e. **secondary corrosion protection** (after breakaway).

The breakdown mechanisms of the primary corrosion protection may be mechanically induced, e.g. by cracks or spallation, or chemically induced. The chemically induced

breakdown is often caused by Cr-depletion of the oxide scale, as a result of Cr-evaporation or other reactions, in combination with an insufficient supply of Cr from the alloy substrate.

The chemically induced breakdown mechanisms of the Cr/Al-rich M_2O_3 oxide scale (i.e. the primary corrosion protection of stainless steels and FeCrAl alloys) have previously been studied by several groups (see e.g [4–7, 9–27, 37, 53, 54, 56, 58, 59]).

One type of breakdown mechanism is by **Cr-evaporation**, occurring either at higher temperatures (>900 °C) through the formation of volatile CrO_3 [60, 61] or e.g. in the presence of water vapour through the formation of $CrO_2(OH)_2$ (see reaction 2.2) [6]. The effects of water vapour on the corrosion of Fe-based alloys have previously been studied extensively and are summarised e.g by Saunders et al. [8].

$$\frac{1}{2}\,Cr_2O_{3(s)} + \frac{3}{4}\,O_{2(g)} + H_2O_{(g)} \rightleftharpoons CrO_2(OH)_2(g) \tag{2.2}$$

Another type of breakdown mechanism is Cr-depletion caused by the formation of **alkali chromates** ($(K/Na)_2CrO_4$) in the presence of different alkali-containing species [18, 56] (see reactions 2.3 and 2.4).

$$\frac{1}{2}\,Cr_2O_{3(s)} + \frac{3}{4}\,O_{2(g)} + K_2CO_{3(s)} \rightleftharpoons K_2CrO_{4(s)} + CO_{2(g)} \tag{2.3}$$

$$\frac{1}{2}\,Cr_2O_{3(s)} + \frac{3}{4}\,O_{2(g)} + H_2O_{(g)} + 2\,KCl_{(s)} \rightleftharpoons K_2CrO_{4(s)} + 2\,HCl_{(g)} \tag{2.4}$$

Pettersson et al. [18], Lehmusto et al. [19], and Jonsson et al. [26], among others, have observed that the breakdown of the Cr-rich oxide is induced in the presence of all of the studied alkali-containing species. A similar type of oxide scale was formed after breakaway, regardless of how the oxide scale broke down (similar to the scale formed in the presence of water vapour or after evaporation of CrO_3). However, the growth rates as well as the compositions of the formed oxide scales were not identical [26, 37]. Therefore, it is possibly that the compositions (and/or microstructures of the alloy and oxide scale) may influence the protective properties of the Fe-rich oxide scale, and the capacity to withstand various corrosive species, such as e.g alkali or chlorine. Systematic studies on the protective properties of the oxide scale formed after breakaway, i.e. the secondary corrosion protection are scarce.

Thus, the focus of this thesis, is on the general aspects of the oxide scales formed after breakaway, i.e. the oxidation properties of the secondary corrosion protection. Less attention is paid to the causes behind the breakdown of the primary corrosion protection. The influences of corrosive species, such as chlorine and alkali, on the secondary corrosion protection represent a topic for future research, although this will be touched on briefly regarding how microstructural changes can influence the oxidation properties.

3

Experimental

3.1 Materials

The materials investigated in this study were Fe-based model alloys, delivered by AB Sandvik Materials Technology, as well as the commercial low-alloyed steel Fe2.25Cr1Mo. The material matrices and compositions of the alloys are presented in Table 3.1, including composition and the expected crystal structure (calculated by H. Larsson from KTH Royal Institute of Technology with the Thermocalc software at equilibrium, 600 °C). The amounts of Cr, Al and Ni were varied separately for all the model alloys, in order to study the influences of alloying elements on the primary- and secondary corrosion protection of FeCr, FeCrNi and FeCrAl.

3.1.1 Production of model alloys

The model alloys were produced at Kanthal AB by induction heating and casting in a Cu-mold under an argon atmosphere. The cast cylindrical ingots were machined, prior to hot rolling, to remove surface defects. The cylinders were heated at 1150 °C and subsequently hot rolled into strip samples (13×3 mm) and reheated approximately four times during the process. The samples were heat-treated after hot rolling, so as to achieve a suitable grain size. The heat treatments were performed at 950 °C (for 1 hour) for the ferritic alloys and 1050 °C (for 30 min) for the austenitic alloys.

3.2 Sample preparation (pre-exposure)

The delivered model alloys were cut into coupons with sample dimensions that ranged from 8×10×2 mm to 15×15×2 mm. The grain sizes of the alloys were investigated by light optical microscopy (LOM) of chemically etched samples. The chemical etching of the FeCr and FeCrAl model alloys was performed at 60 °C in a solution of HCl/H_2O (50:50), while the etching of the FeCrNi model alloys was performed slightly above 60 °C in a solution of $HCl/HNO_3/H_2O$ (45:45:10).

Prior to exposure the, non-etched, metal coupons were ground on SiC paper (P4000), and polished with 3-μm and 1-μm diamond suspensions to a mirror-like appearance. The samples were subsequently de-greased in acetone and ethanol using ultrasonic agitation. Two different types of studies are included in this work (**Paper I** and **Paper II)**. **Paper I**

investigates the influence of KCl(s) on the corrosion of a low-alloyed steel (Fe2.25Cr1Mo) while **Paper II** mainly studies the secondary corrosion protection of FeCr, FeCrNi and FeCrAl model alloys. For these two investigations, two different alkaline salts were sprayed onto the samples prior to exposure. The Fe2.25Cr1Mo steel coupons were sprayed with potassium chloride (KCl(s), 0.1 mg/cm^2) dissolved in ethanol and water (80:20), while the model alloys were sprayed by potassium carbonate (K_2CO_3, 1 mg/cm^2), dissolved in water, to induce break down the primary corrosion protection through the formation of alkali chromates (see reaction 2.3).

FeCr alloys (model alloys) Exposure gas: 5% O_2 + 95% N_2 (bal.)

Alloy	Cr	Ni	Al	Fe	Crystal structure*	Temp. [°C]	Salt
Fe2.25Cr	2.25	-	-	98	Ferrite (BCC)	600	1 mg/cm^2 K_2CO_3(s)
Fe10Cr	10	-	-	90	Ferrite (BCC)	600	1 mg/cm^2 K_2CO_3(s)
Fe18Cr	18	-	-	82	Ferrite (BCC)	600	-/1 mg/cm^2 K_2CO_3(s)
Fe25Cr	25	-	-	75	Ferrite (BCC)	600	1 mg/cm^2 K_2CO_3(s)

FeCrNi alloys (model alloys) Exposure gas: 5% O_2 + 95% N_2

Alloy	Cr	Ni	Al	Fe	Crystal structure*	Temp. [°C]	Salt
Fe18Cr	18	0	-	82	Ferrite (BCC)	600	-/1 mg/cm^2 K_2CO_3(s)
Fe18Cr2Ni	18	2	-	80	Ferrite (BCC)	600	-/1 mg/cm^2 K_2CO_3(s)
Fe18Cr3Ni	18	3	-	-	Ferrite (BCC)	600	-/1 mg/cm^2 K_2CO_3(s)
Fe18Cr5Ni	18	5	-	77	90:10 (BCC/FCC)	600	-/1 mg/cm^2 K_2CO_3(s)
Fe18Cr10Ni	18	10	-	72	50:50 (BCC/FCC)	600	-/1 mg/cm^2 K_2CO_3(s)
Fe18Cr16Ni	18	16	-	-	Austenite (FCC)	600	-/1 mg/cm^2 K_2CO_3(s)
Fe18Cr20Ni	18	20	-	62	Austenite (FCC)	600	-/1 mg/cm^2 K_2CO_3(s)
Fe18Cr34Ni	18	34	-	48	Austenite (FCC)	600	-/1 mg/cm^2 K_2CO_3(s)
18Cr81Ni	18	81	-	1	Austenite (FCC)	600	-/1 mg/cm^2 K_2CO_3(s)

FeCrAl alloys (model alloys) Exposure gas: 5% O_2 + 95% N_2

Alloy	Cr	Ni	Al	Fe	Crystal structure*	Temp. [°C]	Salt
Fe5Cr3Al	5	-	3	92	Ferrite (BCC)	600	-/1 mg/cm^2 K_2CO_3(s)
Fe10Cr3Al	10	-	3	87	Ferrite (BCC)	600	-/1 mg/cm^2 K_2CO_3(s)
Fe18Cr3Al	18	-	3	79	Ferrite (BCC)	600	-/1 mg/cm^2 K_2CO_3(s)
Fe18Cr1Al	18	-	1	81	Ferrite (BCC)	600	-/1 mg/cm^2 K_2CO_3(s)
Fe18Cr6Al	18	-	6	76	Ferrite (BCC)	600	-/1 mg/cm^2 K_2CO_3(s)
Fe25Cr3Al	25	-	3	72	Ferrite (BCC)	600	-/1 mg/cm^2 K_2CO_3(s)

Fe2.25Cr1Mo (commercial) Exposure gas: 5% O_2 + 20% H_2O + N_2 (bal.)

Alloy	Cr	Mo	Fe	Crystal structure	Temp. [°C]	Corrosive species
Fe2.25Cr1Mo	2.25	1	98	Ferrite (BCC)	400	Reference (no chlorine)
Fe2.25Cr1Mo	2.25	1	98	Ferrite (BCC)	400	+ HCl(g) (500vppm)
Fe2.25Cr1Mo	2.25	1	98	Ferrite (BCC)	400	+ KCl(s) (0.1 mg/cm^2)
Fe2.25Cr1Mo	2.25	1	98	Ferrite (BCC)	400	+ KCl(s) + HCl(g)

*Table 3.1: Exposure matrices and nominal compositions for all the investigated alloys, and the crystal structures of the model alloys, *calculated at equilibrium (600 °C=exposure temperature) by H. Larsson (KTH) using the Thermocalc software (TC).*

3.3 Furnace exposures

The furnace exposures were carried out on metal coupons in a horizontal tube furnace, as well as using thermogravimetric analysis (TGA). The TGA records the mass gain in-situ, providing insights into the oxidation kinetics, as well as additional mechanisms such as evaporation and crack formation. The TGA used in this work was a Setaram Setsys thermobalance humidified with a Setaram Wetsys (for wet exposures). The samples were positioned parallel to the direction of the gas flow in both furnace set-ups and all parts of the systems were maintained above the dew-point of water (wet exposures), to prevent condensation.

The Fe2.25Cr1Mo steel coupons were exposed for 24 hours at 400 °C in 5% O_2 + 20% H_2O + N_2 (bal.) with and without HCl(g) and/or KCl(s) in both the tube furnace and the TGA. The model alloys were exposed at 600 °C in 5% O_2 + 95% N_2 with and without K_2CO_3. The exposures in the presence of K_2CO_3 were performed in both the tube furnace and the TGA. The exposure conditions are summarised in Table 3.1. All the alloys were exposed both with and without the salt deposited onto the samples.

The gravimetric measurements were carried out using a Sartorius balance with micro-gram resolution. All samples were stored in desiccators (drying agent P_2O_5) prior to exposure and while awaiting analysis, to avoid atmospheric corrosion and potential hygroscopic effects of chlorine-containing species and K_2CO_3. Estimated oxide scale thicknesses, x, were calculated from the mass gain data (W [g/cm^2]) for each alloy, so as to link the mass gain study with the microstructural investigation (see Eq. 3.1). The calculation was performed under the assumptions that the oxide scale was dense, composed of one pre-defined oxide (M_aO_b) with density ρ, and that the measured mass gain accounted for only oxygen uptake that resulted in oxide formation.

$$x = \frac{W}{\frac{aM_O}{aM_O+bM_M}\rho} \tag{3.1}$$

The furnace exposures and TGA measurements in this work were performed mainly by PhD student Johan Eklund, Dr. Erik Larsson, and MSc student William Fung. A few exposures were performed by Dr. Mercedez Andrea Olivas Ogaz, PhD student Julien Phother Simon and BSc student Emile Sechaud.

3.4 Sample preparation (post-exposure)

After exposure, a few selected samples were prepared for cross-sectional analyses in the scanning electron microscope (SEM) and transmission electron microscope (TEM). The sample preparation was performed using two different ion-milling tools, namely broad ion beam (BIB) and focused ion beam (FIB). The FIB was also used to image the cross-sections with ions, described more in detail in Section 4.1.4.

3.4.1 Broad ion beam (BIB)

The BIB is a technique used to produce wide, ion-milled cross-sections, so as to generate surfaces that are suitable for surface-sensitive ion and electron microscopy. The technique applies a broad beam of argon (Ar) ions in order to sputter away material from the sample, resulting in millimetre-wide cross-sections. Although, BIB milling is not as precise as FIB, it enables the analysis of larger areas.

In this work, the BIB was used to prepare wide cross-sections of the Fe-rich oxide scales formed in the secondary corrosion regime. The instrument used was the Leica EM TIC 3X Ion beam milling system equipped with a triple Ar ion gun and operated at 4-8 kV. The higher accelerating voltages (6.5-8.0 kV) were used for coarse milling, while, for some samples, the final milling was performed at 4 kV to generate an improved surface for low-keV SEM imaging. Prior to milling, the samples were cut, without lubrication, using a low-speed saw. The exposed coupons were sputtered with gold and covered with a 0.5-mm-thick silicon wafer prior to cutting, so as to protect the oxide scale from spalling. Preparation of the BIB milled cross-sections in this work was carried out in paert by PhD student Johan Eklund, Dr. Erik Larsson and MSc student William Fung.

3.4.2 Focused ion beam (FIB)

FIB is a technique that can be used either for microscopy or as a milling tool (see Figure 3.1a). In this work, the FEI Versa3D LoVac DualBeam instrument was used to produce well-defined, one-sided cross-sections for SEM analysis, as well as electron-transparent lamellae for TEM analysis through an *in situ* lift-out procedure (described in detail below). The instrument is a combined FIB and SEM (mounted at an angle of 52° to each other) equipped with a Ga liquid metal ion source (LMIS), detectors for secondary electrons and ions (eSEs, iSEs) and backscattered electron (BSE), a Gas Injection System (GIS) for the deposition of Pt, and an Omniprobe needle for lift-out of the thin TEM lamellae. The GIS is used to inject gas into the sample chamber, directed towards a specific region of the sample, which makes it possible to deposit a protective coating onto the area of interest, as illustrated in Figure 3.1b.

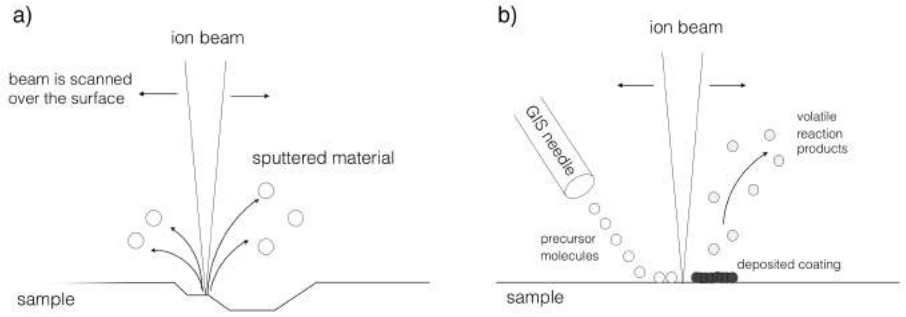

Figure 3.1: Illustration of: a) the milling principle and b) the ion-assisted GIS deposition in the FIB (reconstructed from [62]). The ion beam interacts with a) the sample (to sputters away material) or b) precursor gases (from the GIS) adsorbed on the sample surface (to generate reaction products that form a deposited layer).

The *in situ* lift-out procedure used to produce thin lamellae for TEM investigations is illustrated in Figure 3.2. During the lift-out procedure, the electron column is used for monitoring, while the ion column is used for milling. Both the electron and ion columns are used with the GIS to deposit Pt. The Pt, which is used as a weld and as protection from ion bombardment, reduces ion implantation and an artefact of the cross-section called 'curtaining'. The lift-out procedure is carried out in several steps and starts by locating the precise position of the milling (Figure 3.2a). The GIS needle is used to deposit a thin protective Pt strip onto the area of milling (Figure 3.2b-c), assisted by electrons (to reduce the risk of ion implantation) and ions (for more efficient deposition). The sample is tilted an angle of 52° (sample surface normal to the ion column) and trenches are milled at high beam currents ($\sim$ 15 nA) on both sides of the Pt strip (Figure 3.2d). The material beneath and on the sides of the trenches is milled away ('u-cut') with lower beam currents (3-5 nA) at a tilt angle of 0° tilt, leaving only one side of the lamella attached to the original sample. The Omniprobe needle is inserted, and Pt is used to weld the other side of the lamella onto the Omniprobe. The remaining material attached to the original sample is removed using low beam current (3 nA) ion milling to reduce re-deposition. When the lamella is attached to the Omniprobe needle, the stage is lowered and the lamella is welded onto a Cu grid by Pt deposition. The attachment on the Omniprobe needle is milled away (beam current, 1-3 nA) and the lamella is thinned down, as to produce an electron-transparent specimen ($\sim$ 100 nm), for the TEM analyis (Figure 3.2e). The thinning of the sample requires careful and precise milling. Thus, the thinning is performed by ion milling using gradually lowered beam currents (1 nA, 0.3 nA, 100 pA) on both sides of the lamella. In the final thinning (100 pA), the milling is made on both sides simultaneously, in order to reduce the risk of bending of the thin lamella. A final electron-transparent lamella, mounted on the Cu-grid, is shown in Figure 3.2e.

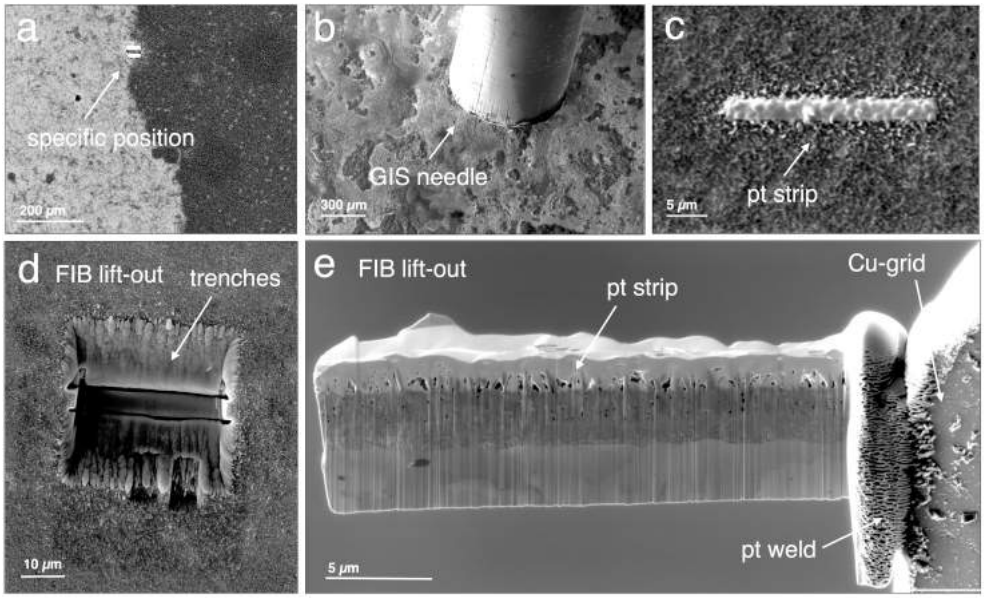

Figure 3.2: Illustration of the lift-out procedure performed in the FIB/SEM system. A precise location is chosen (a), Pt is deposited (b-c), trenches are milled and a thin lamella is extracted and welded onto a Cu grid (d-e). The specimen is thinned down, resulting in an electron-transparent foil suitable for TEM analysis (e).

4

Analytical techniques

Oxide scales formed on alloys exposed at high temperatures exhibit different properties. To understand the corrosion mechanisms at play and how the protective properties of different oxides may vary, a thorough investigation of the oxide microstructures and chemical compositions is necessary. For a detailed microstructural investigation it is preferential to use a combination of different characterisation techniques, that provide complementary data on the elemental composition and distribution, surface morphology and crystal structure of the formed oxides. Figure 4.1 illustrates the strategy for the analysis of oxide scales and the importance of combining advanced and more simple analysis techniques to increase the understanding of corrosion processes.

The oxide scales in this work were imaged and analysed using a combination of ion and electron microscopy techniques (SEM, FIB, TEM), as well as by x-ray spectroscopy (EDX) and diffraction (XRD, TKD). Other techniques, such as e.g. atom probe tomography (APT), electron energy loss spectroscopy (EELS) and high-resolution TEM (HR-TEM) could also be used to characterise the oxides in more detail. However, these techniques were not used in this work. This chapter presents all the analytical techniques used in the investigation and briefly explains the underlying physics underlying the detected signals, so that the reader can understand and appreciate the specific information obtained from each technique.

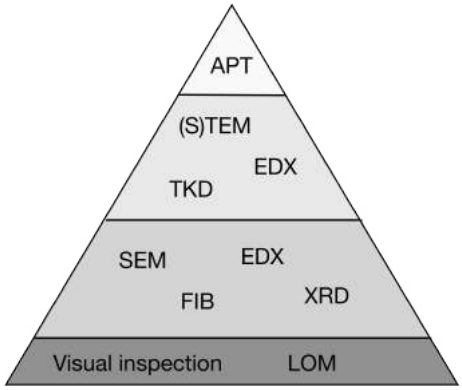

Figure 4.1: Illustration of the strategy used in this work to combine different techniques to gain statistics and analysis of representative samples for a large range of scales (cm to Å).

4.1 Imaging

4.1.1 Light optical microscopy (LOM)

Light optical microscopy (LOM) and visual inspection are often useful as the starting points for investigating a material. In light optical microscopy, a beam of photons is focused on the sample and the scattered photons are converted to an image *via* magnifying lenses. The spatial resolution of the image obtained using a light optical microscope is determined by the wavelength of the incident photons, which are in the order of $\sim 10^2$ nm. To distinguish and image smaller features on the investigated samples, a higher spatial resolution is required. Since the wavelength of electrons is much shorter than the wavelenght of light, electron microscopy can be used for this purpose.

4.1.2 Scanning electron microscopy (SEM)

Scanning electron microscopy is a technique (SEM) in which images are produced by rastering a focused beam of electrons over the sample surface, so as to generate signals that originate form beam-specimen interactions. The signals are detected and converted to obtain high-resolution images of a few nanometres, which provide information about the surface topography, density and chemical composition [63]. The high spatial resolution and large depth of field are two of the main advantages of SEM compared to LOM.

A schematic of a SEM can be seen in Figure 4.2. The SEM comprises three main parts: the electron gun, in which the electron beam is generated and accelerated; the electron column where the beam is controlled by electromagnetic lenses; and the sample chamber, in which the electron-specimen interactions are detected. In order to obtain high-quality images in the SEM, the electron beam should be focused onto the sample with the smallest possible probe size while maintaining a high electron current. This is achieved by using a set of electromagnetic lenses and apertures through which the accelerated electrons pass before reaching the specimen. The main electromagnetic lenses in the electron column are the condenser lens and the objective lens, while scanning coils are used to raster the beam over the specimen. The condenser lens converges the electron beam to obtain a small probe size, while the objective lens is used to focus the electron beam onto the sample [63].

The beam-specimen interactions in the SEM generate various types of signals. In this work the secondary electrons (SEs), backscattered electrons (BSEs) and characteristic x-rays are used. The different signals are detected from different depths of the specimen, as illustrated by the interaction volume in Figure 4.3. This is explained by the fact that SEs, BSEs and x-rays have varying abilities to escape from the specimen (i.e. different escape depths), resulting in varying spatial resolutions of the different signals.

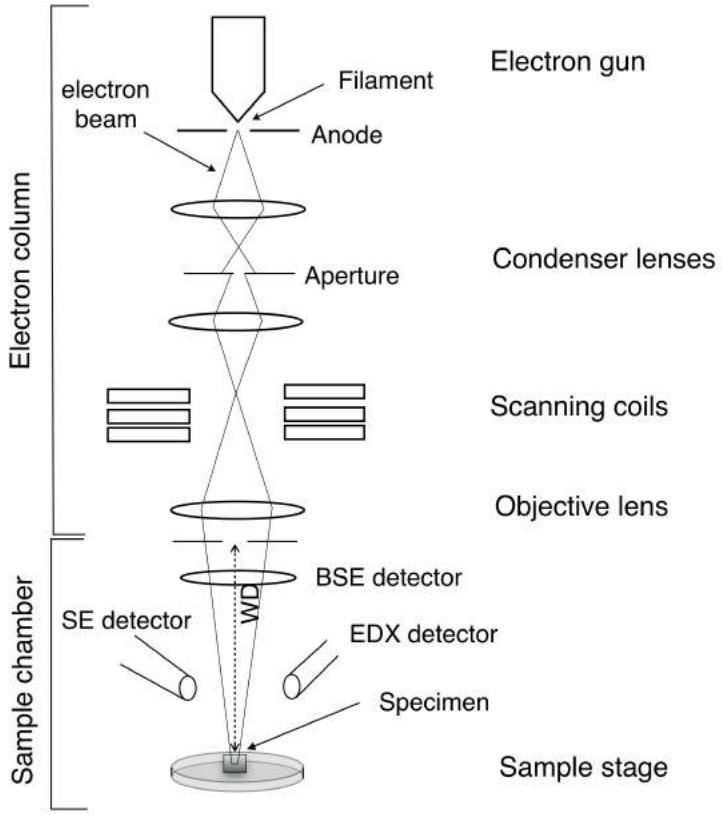

Figure 4.2: Schematic of a SEM. The figure is composed from the descriptions in [63]. Note that the design and beam cross-over may differ depending on the type of SEM used.

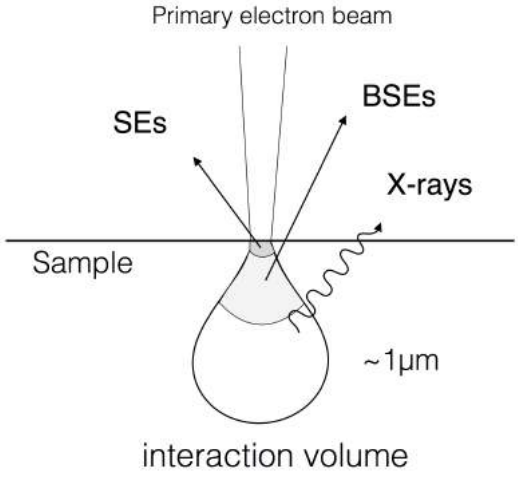

Figure 4.3: Illustration, based on the description in [63], of the interaction volumes resulting from different escape depths of the detected signals in the SEM. The size and shape of the interaction volume depends on the specimen and the accelerating voltage; it is in the order of ∼1µm for characteristic x-rays at ∼ 20 keV.

The **secondary electrons (SEs)** are low-energy electrons (<50 eV), ejected from the

specimen (see Figure 4.4a). The small interaction volume of SEs (short escape depth, see Figure 4.3) results in surface sensitive images with a spatial resolution of up to a few nanometers. The short escape depth also results in enhanced topographical contrast in SE images due to the so called 'edge effect'.

The **backscattered electrons (BSEs)**, on the other hand, are elastically scattered electrons (see Figure 4.4b) with energies similar to that of the primary electrons ($\sim$ 10-20 keV). Thus, the BSEs can escape from larger depths of the specimen, resulting in poorer spatial resolution (a few hundreds of nanometres). The amount of BSEs generated is proportional to the atomic number (Z) and the density of the sample [63]. Thus, the BSE images contain information about both density and composition, reflected as brighter (dense/higher Z) and darker (porous/lower Z) regions in the image. In this work, the compositional contrast of BSEs is also used for qualitative determinations of the thicknesses and distributions of oxide scales grown on the metal coupons. If the accelerating voltage is set high enough for the interaction volume to reach the metal substrate beneath the oxide, a thin oxide scale will result in more BSEs being generated from the metal substrate. Thus, the BSE contrast results in images with brighter regions for thin, as compared to thick, oxide scales.

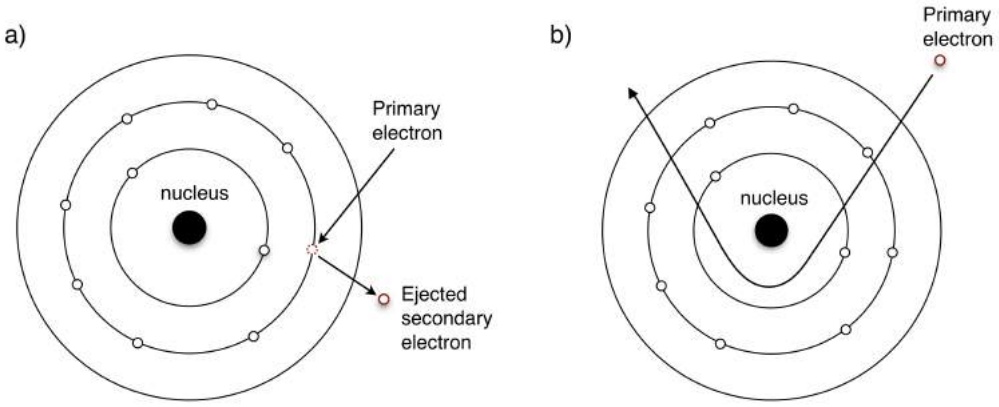

Figure 4.4: Illustration of the principles underlying the generation of: a) secondary electrons (SEs); and b) backscattered electrons (BSEs), based on the description in [63].

In this work, the SEM was used in combination with Energy dispersive x-ray spectroscopy (EDX) to investigate the morphology and composition of the surface, as well as to examine the wider cross-sections prepared by BIB milling. This is of great importance in order to ensure that the samples chosen for the TEM analysis are representative for the overall corrosion of the samples. The SEM analysis was performed in an FEI Quanta ESEM 200 and a Zeiss LEO Ultra 55 FEG SEM, operated in high vacuum mode. Both microscopes are equipped with a field emission gun and were operated at accelerating voltages of 1.5-2.0 keV for surface-sensitive imaging in the Zeiss LEO Ultra 55 FEG SEM, 10-30 keV for imaging in the FEI Quanta ESEM 200, and 15-25 keV for the chemical analysis. Both secondary electrons (SEs) and backscattered electrons (BSEs) were used for imaging. The low-keV imaging was used with an in-lens detector in the Zeiss LEO Ultra 55 to obtain high-resolution images, as well as to determine the sizes of small oxide grains on the ion-etched samples (for details, see Figure 4.8c and Section 4.1.4).

4.1.3 Transmission electron microscopy (TEM)

Transmission electron microscopy (TEM) has the ability to provide imaging and chemical analysis with high spatial resolution (∼Å), as well as crystallographic information for specific positions of the sample studied [64]. The principle of imaging in the TEM is different from that of the SEM in that the image is formed by the electrons that are transmitted through the specimen. In order for the electrons to pass through the specimen, the samples need to be electron-transparent (thickness of ∼ 100 nm) at the operating accelerating voltage (∼ 200-300 keV).

The TEM can be operated either in conventional TEM mode or in scanning TEM (STEM) mode. The design of the TEM is rather similar to that of the SEM and FIB, in particular in STEM mode. The primary electrons are generated and accelerated in the electron gun and pass through a set of electromagnetic lenses, apertures, and scanning coils (for STEM), before reaching the sample. In contrast to the SEM and FIB, the electron interactions for imaging in the TEM are detected below the sample where the transmitted electrons pass through additional electromagnetic lenses to further magnify the image [64].

The transmitted electrons either pass straight through the sample or are scattered within the sample, enabling different imaging modes (see Figures 4.5 and 4.6). The imaging mode for detecting un-scattered electrons is called **bright-field (BF) mode**. In BF mode, the image is produced by the un-scattered electrons, and the scattered electrons are efficiently filtered out by the objective aperture. This results in images in which regions that give rise to less electron scattering appear brighter, e.g. thinner regions, holes and elements of lower atomic number, (see Figure 4.5a) [64]. In contrast, the **dark-field (DF) mode** is created by the scattered transmitted electrons, such that thin areas and holes, which scatters fewer electrons, will appear dark, while denser regions or materials with higher atomic numbers will appear bright.

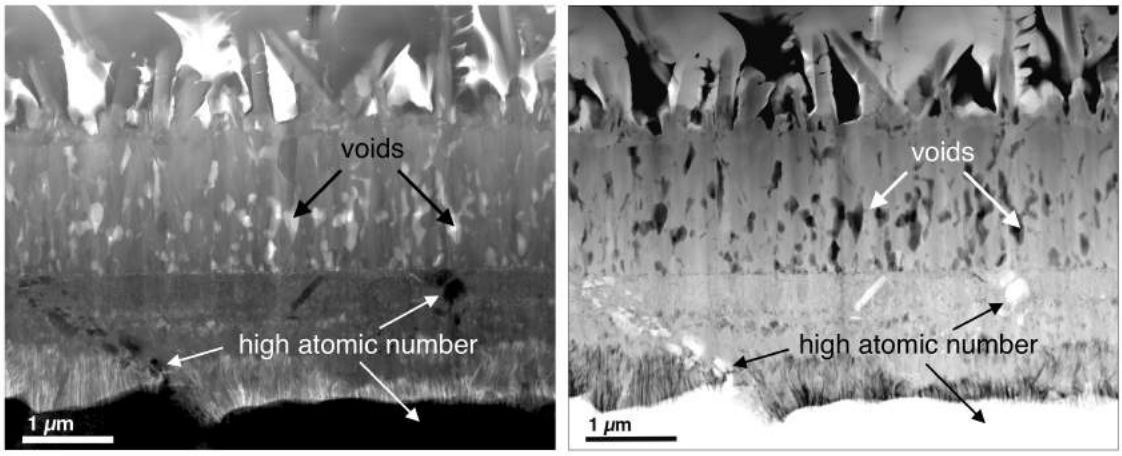

Figure 4.5: Examples of a) bright field imaging and b) dark field imaging using STEM. The TEM was operated by Dr. Mohammad Sattari.

Different detectors are used to detect the scattered transmitted electrons and to enhance certain contrasts. In STEM mode, a DF image may be produced by an annular dark field detector (ADF), which is sensitive to scattered electrons from a specific range of angles (see Figure 4.6). The scattering intensities at high scattering angles are strongly dependent upon the atomic number, which results in enhanced compositional contrast for high scattering angles, with heavier elements appearing bright, in contrast to the BF imaging mode [64]. This is the working principle of the High-Angle Annular Dark-field (HAADF) detector (see Figure 4.5b).

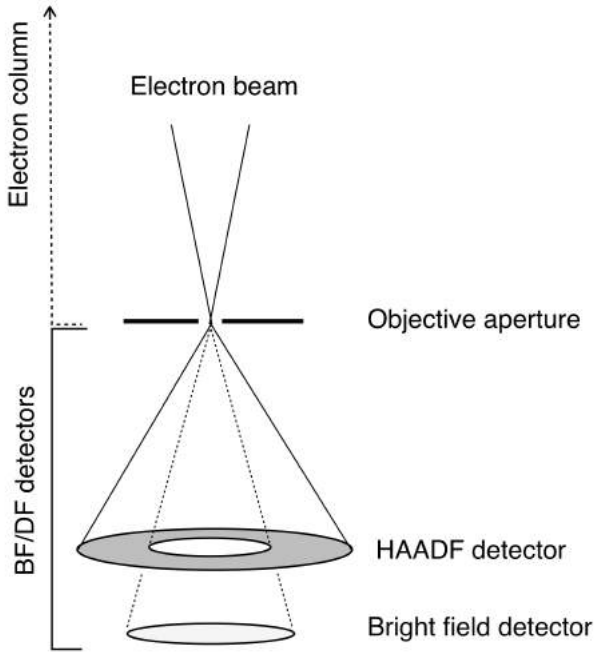

Figure 4.6: Schematic of the BF and HAADF detectors in the TEM from descriptions in [64,65].

In this work, an FEI Titan 80-300 TEM was used, equipped with a field emission gun, and an Oxford X-sight EDX detector. The TEM was used in STEM mode, both in the BF and HAADF imaging modes. The chemical analysis performed in the TEM was performed using STEM/EDX. The operation of the TEM was partly performed by Dr. Mohammad Sattari at Chalmers University of Technology.

4.1.4 Focused ion beam (imaging mode)

The principle of the FIB used as a microscope (imaging mode) is similar to that of the SEM, with the difference being that the FIB uses ions, instead of electrons, as the incident beam. Image formation is based on the same principles as the SEM, and the resolution of the FIB is in the same order of magnitude, albeit slightly lower than that of SEM. The design of the FIB is similar to that of the SEM. Thus, ions are generated in an ion source (Ga LMIS) and pass through a set of electrostatic lenses and scanning coils, to focus and raster the ion beam onto the sample (see Figure 4.7a) [66, 67].

The FIB used in this work is a dual-beam workstation, combining a FIB and an SEM,

whereby the electron column and the ion column are mounted at an angle of 52° to each other (see Figure 4.7b). Imaging in the FIB/SEM workstation can be performed either using an incident ion beam (FIB) or an electron beam (SEM), and the principle of image formation in the FIB is similar to that of the SEM, as illustrated in Figure 4.7. The incident ion beam interacts with the specimen, resulting in emitted SEs (iSEs) and secondary ions (iSIs) which can be detected to form an image [66]. Ion-induced SE imaging (iSE) is a common imaging mode in the FIB, due to its higher spatial resolution and yield compared to secondary ion (SI) imaging [66, 67]. However, the spatial resolution of of ion induced SEs (iSEs) is still lower than that of electron-induced SEs.

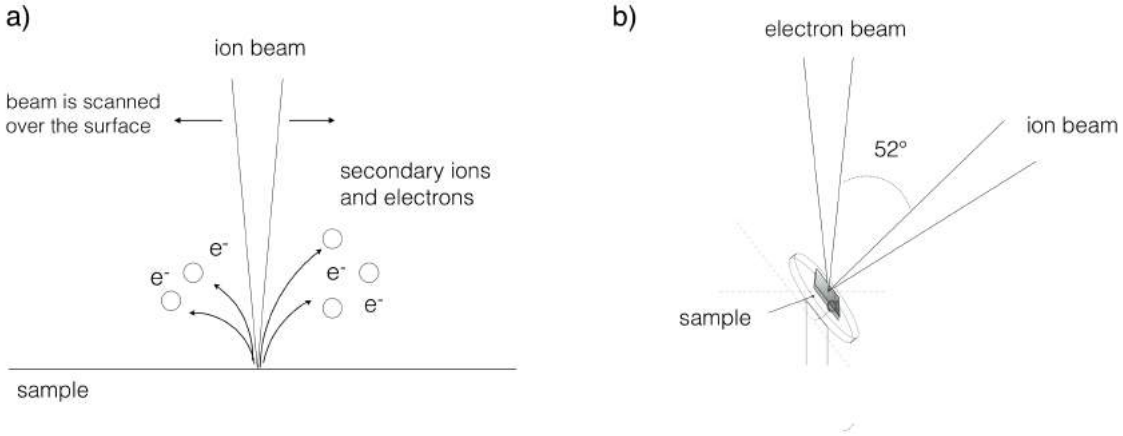

Figure 4.7: Illustration of the image formation in the FIB (a), as reconstructed from [62], and b) a schematic of the SEM/FIB workstation.

The drawbacks of using FIB in imaging mode include its lower spatial resolution, as compared to SEM, and the fact that it is a destructive technique due to the highly energetic incident ions that will sputter away material from the sample and may cause ion implantation even at low beam currents. However, a strong advantage of FIB used for imaging is that a contrast mechanism called 'channelling contrast' is enhanced in ion microscopy (for example, see Figure 4.8b). Channelling contrast is based on the principle that crystal lattice planes aligned with the ion trajectory will channel more ions, resulting in a lower SE yield. Thus, when imaging polycrystalline samples, the channelling contrast will produce images in which the grains oriented in the ion trajectory appear darker (low SE yield), while the grains in other orientations appear brighter (see example in Figure 4.8a-b) [62, 66]. In this work, FIB-imaging was primarily used to image the oxide grains. The instrument was operated in high vacuum mode at an acceleration voltage of 30 keV and a beam current of 10 pA. In order to obtain better grain contrast, the cross-sections were imaged several times in a row using ion induced secondary electrons (iSEs). This repetitive ion imaging resulted in ion-etching of the oxide grains, which was used as an asdditional sample preparation technique for imaging small oxide grains with low-keV SEM (see Figure 4.8c). The oxide grain sizes are measured in an orientation normal to the growth direction of the oxide scale, assuming that these grain boundaries are the most relevant pathways for ion diffusion.

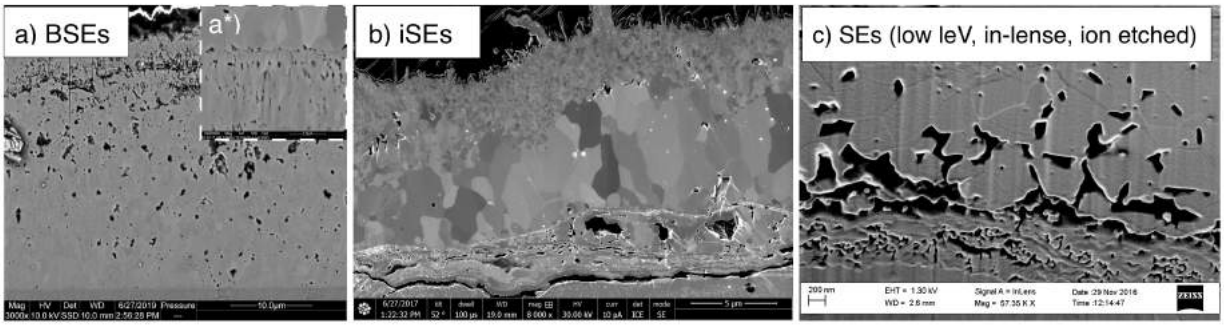

Figure 4.8: Examples of different imaging techniques to image oxide grains. a) BSE imaging (channeling contrast), b)iSE imaging (enhanced channeling contrast), c) low keV SE imaging on an ion-etched surface. The insert in a) (a) shows how an improved surface may enable for better grain contrast also in BSE mode.*

Tilting the sample may enhance the channelling contrast. However, when producing images of tilted samples, the tilting angle, relative to the electron or ion column, must be taken into account and the thickness of the oxide scale or grain size measured in the image must be re-calculated using Eq. 4.1, where T is the real thickness, T_0 is the measured thickness (image), and α is the tilt angle (relative to the horizontal plane) (see Figure 4.7b).

$$T = \frac{T_0}{\sin \alpha} \tag{4.1}$$

4.2 Chemical analysis

4.2.1 Energy dispersive x-ray spectroscopy (EDX)

Energy dispersive x-ray spectroscopy (EDX) is a powerful tool for chemical analysis of oxide scales [63, 64]. EDX uses characteristic x-rays that are generated when the primary electron beam interacts with the specimen, as illustrated in Figure 4.9. The primary electrons eject low-energy (inner shell) from the specimen, thereby exciting the atom. The atom relaxes by that electrons from a higher energy level (outer shell) re-occupies the electron hole in the 'inner shell', during which process characteristic x-rays may be generated. The generated x-rays have specific energies corresponding to the difference between the two energy levels, and are characteristic of the atom from which they were generated. The beam-specimen interactions will not only generate characteristic x-rays, but also a continuous x-ray spectrum (bremstrahlung), generated by the fact that interactions with free and loosely bound electrons will slow down the primary electrons. Thus, the generated X-ray spectrum contains both the background signal (bremstrahlung) and the discrete characteristic x-ray lines (see example in Figure 4.9).

Characteristic x-rays can escape from a larger volume of the sample than can SEs or BSEs, which means that EDX analysis in the SEM has a poorer spatial resolution, as illustrated in Figure 4.3 [63]. The size of the interaction volume in the SEM depends both on the type of specimen and the accelerating voltage, with lower accelerating voltages resulting in smaller interaction volumes. However, the accelerating voltage must still

be sufficiently high to eject the inner shell electrons, so as to generate the characteristic x-rays. In STEM/EDX analysis, the low sample thickness of the TEM lamella results in an insignificant interaction volume, and EDX analysis with higher spatial resolution. The spatial resolution of the STEM/EDX analysis is within the order of nanometres, as compared to the micrometre resolution obtained on bulk samples in the SEM/EDX [64].

Quantitative EDX analysis is performed by filtering out the background signal and integrating the area of the characteristic x-ray peaks. The accuracy of quantitative EDX analysis depends on several factors both regarding x-ray yield, sample homogeneity, data processing or errors associated with the standards used for the quantification [63]. The ZAF-correction is commonly used in order to compensate for some of factors, such as the effects of electron scattering for different atomic numbers (Z), the the absorption of x-rays within the specimen (A), and the fluorescence effect (F) that results from the generated x-rays from one type of atom exciting surrounding atoms. In the STEM/EDX, the thin samples result in greatly reduced absorbance and fluorescence effects, which is used in the thin-foil criterion, simplifying the quantification by assuming that factors A and F can be ignored [64]. However, it must be mentioned that the absorbance and fluorescence effects are enhanced for thicker specimens (thicker foils), also in the TEM, and that different atoms may be more or less sensitive to the factors mentioned. Therefore, in both the STEM/EDX and SEM/EDX analyses, caution must be exerted in the quantification. If possible, a sample with known composition, should be quantified as a reference before starting the EDX analysis. Another aspect of the EDX analysis that needs to be considered is that the quantification of lighter elements, such as e.g. oxygen, is poor. Thus, in this work, oxygen is excluded from the quantification, and only cations are quantified. An alternative solution to this problem is to perform standard EDX analysis, to obtain a better quantification of, for example oxygen, using known standards and non-normalised quantification.

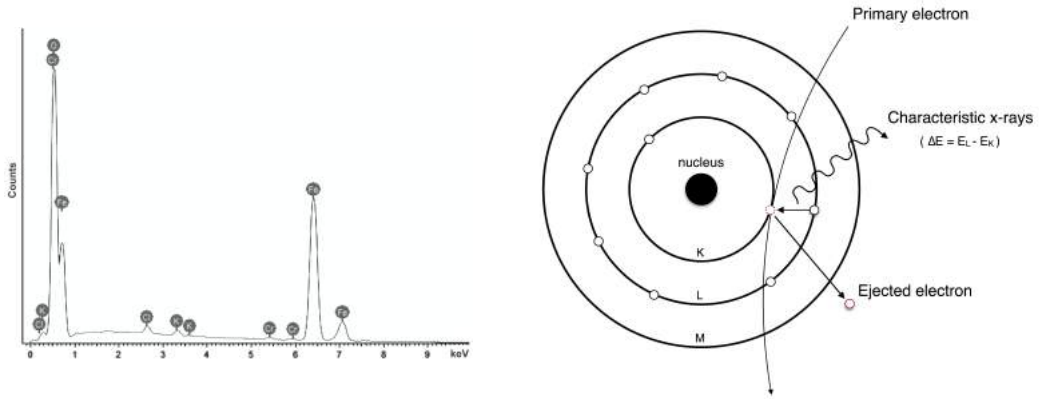

Figure 4.9: Illustration of EDX analysis; Left: Example of an EDX spectrum, containing characteristic x-rays and background signal (bremsstrahlung). Right: Illustration of the generation of the characteristic x-rays used for EDX analysis, based on description in [63].

In this work, EDX is used both in the SEM and in STEM, resulting in chemical analyses with different spatial resolutions, due to the reduction in interaction volume that occurs

from bulk (SEM) to thin-foil (TEM) samples. Thus, the chemical analysis is more local for the STEM/EDX than for the SEM/EDX. There are both advantages and disadvantages associated with the deployment of each of these techniques, and the combination of the two techniques provides complementary information. The EDX detector used in the SEM was an Oxford X-max 80 EDX, while an Oxford X-sight EDX detector was used in the TEM. The quantification was made in the Oxford Inca software for the SEM/EDX and the TIA software for the STEM/EDX.

4.3 Diffraction

4.3.1 X-ray diffraction (XRD)

X-ray diffraction (XRD) is used to determine the crystal structures of crystalline materials [68]. The technique is based on the Bragg diffraction resulting from incident x-rays that interact with the crystal lattice. Bragg diffraction occurs at discrete angles according to Bragg's law: $2d \sin\theta = n\lambda$, where n is a discrete integer, θ the incident angle, λ the x-ray wavelength, and d is the distance between the atomic planes in the crystalline material. By measuring the angles and intensities of the bragg diffracted beams, the crystal structure of the sample can be determined. In the present work, the oxide crystal structures were characterised using a Siemens D5000 powder x-ray diffractometer with a CuK_α source (λ=1.5418 Å). The instrument was operated in grazing incidence geometry with an angle of incidence between 0.5 - 4.0° and a measuring range of $10° < 2\theta < 85°$. The XRD measurements in this work were performed with the assistance of PhD student Johan Eklund at Chalmers University of Technology.

4.3.2 Electron diffraction (TKD and TEM)

In addition to imaging and chemical analyses, the electron interactions that take place in crystalline materials also result in electron diffraction according to Bragg's law (see above, where λ refers to the de Broglie wavelength of the electrons). Thus, the SEM and TEM allow for the detection and visualisation of the crystal structures and e.g. grain orientations of materials. In the SEM, the crystallographic information and grain orientation can be obtained by electron backscatter diffraction (EBSD) or transmission kikuchi diffraction (TKD). Both techniques are based on the same principle (and use the same type of detector). However, EBSD is performed on bulk samples, thereby limiting the resolution according to the electron interaction volume [69], whereas TKD is performed on thin-foil samples. In the TEM, two different diffraction modes are possible: i) selected area electron diffraction (SAED); and ii) convergent beam electron diffraction (CBED), producing spot- and disc-based diffraction patterns respectively [64]. In this work, electron diffraction in the TEM was used only in a qualitative manner, in order to decide whether or not certain regions were crystalline, whereas the TKD was used on one oxide scale to confirm the presence of hematite (Fe_2O_3). The TKD was operated by Pat Trimby of Oxford Instruments.

5

Results & discussion

This chapter implements the concept of primary and secondary corrosion regimes, as presented in Chapter 2, for three material classes (low-alloyed steels, stainless steels, FeCrAl alloys). The results include studies on the corrosion of a commercial low-alloyed steel (Fe2.25Cr1Mo) exposed at 400 °C (**Paper I**) and Fe-based model alloys exposed at 600 °C (**Paper II**), see Table 3.1.

5.1 Corrosion regimes in high temperature corrosion

The corrosion protection of stainless steels and FeCrAl alloys rely on the formation of a slow-growing Cr- and/or Al-rich M_2O_3 oxide scale formed in mildly corrosive environments [1–3]. In harsher environments, these oxide scales may break down (breakaway corrosion) and a faster-growing, multi-layered, Fe-rich oxide scale is then formed.

The oxide scale formed after breakaway corrosion has previously been studied by several groups (see e.g. [9, 10, 12, 13, 23, 25–27, 37]). The focus of most previous studies have been to increase the understanding, so as to prevent or delay the primary corrosion protection from breaking down. Therefore, previous studies on the protective properties of the oxide scale formed after breakaway are scarce. However, a few studies (see e.g. [25, 37]) have indicated that the protective properties of the scale formed after breakaway may be improved, for example by altering the alloy composition. Thus, to be able to systematically investigate the protective properties and to characterise the corrosion attack described in previous studies, the present work implements the concept of primary and secondary corrosion regimes for the corrosion protection before and after breakaway, respectively. This concept is used as a means to study the corrosion of materials from the perspective of which type of oxide scale that is formed in a certain type of environment. The terminology is considered important for material developers and for the development of oxidation modelling tools. It is also of great interest in terms of the selection of materials for use in high temperature applications, specifically for those applications in which breakaway corrosion cannot be prevented, such as biomass- and waste-fired boilers.

This work mainly focuses on the oxidation properties of the oxide scale formed after breakaway (i.e. the secondary corrosion regime) and how microstructural differences may influence the growth rate of the Fe-rich oxide scales. Increased knowledge of how the oxidation properties of the secondary corrosion protection vary for different materials is

the first step towards understanding the corrosion propagation of different materials also in even more corrosive environments.

In general, the corrosion mechanisms before and after breakaway are considered to be fundamentally different. The different corrosion regimes are schematically illustrated in terms of the oxidation kinetics in Figure 5.1. The primary corrosion regime (see A_1) refers to the formation of a slow-growing, M_2O_3 oxide scale, which may break down (in the presence of e.g. K_2CO_3) to form a faster-growing, Fe-rich oxide, i.e. the secondary corrosion regime (see A_2). The results of this work show that the incubation time to breakaway varies (see curves A, B), as do the growth rates of the primary corrosion protection (see A_1, D) and secondary corrosion protection (see A_2, B, C), as illustrated in Figure 5.1.

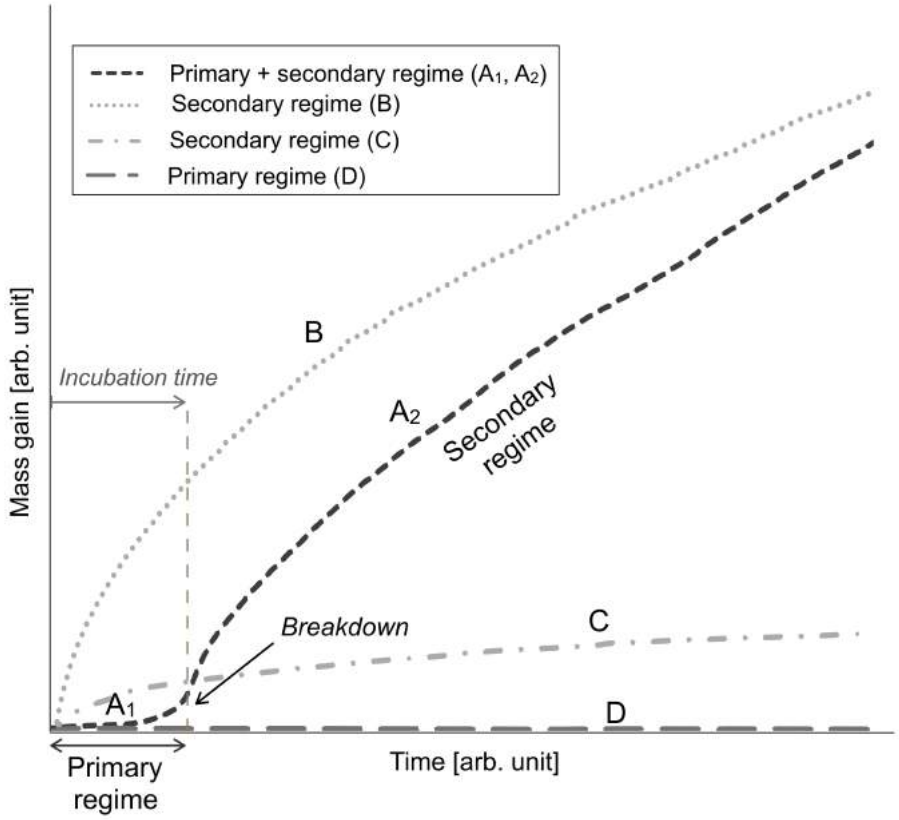

Figure 5.1: Illustration of the primary (A_1, D) and secondary (A_2, B, C) corrosion regimes of Fe-based alloys. The primary and secondary regimes (A_1 and A_2, respectively) are indicated in the figure along with the breakaway event and incubation time. Note that the breakaway event occurs instantly in curves B and C, and that the growth rate may be different both in the primary and secondary corrosion regime.

Figure 5.2 shows the gravimetric results for the FeCr, FeCrNi, and FeCrAl model alloys, exposed for 24 hours at 600 °C (5% O_2 + 95% N_2) in the absence and presence of K_2CO_3(s). The K_2CO_3(s) was used to break down the primary corrosion protection, to allow investigation of the secondary corrosion regime without the influence of other corrosive species, such as e.g. chlorine. Most of the alloys exposed in the absence of K_2CO_3 (i.e. a mild environment) show mass gains indicating thin oxide scales (W_{1st} <0.35 mg/cm^2)

while all of the alloys, except for Fe18Cr6Al, exposed to K_2CO_3 show comparatively high mass gains ($W_{2nd} \approx$ 10-500 $\times$ W_{1st}). Thus, the gravimetric results clearly illustrate the two corrosion regimes before (primary regime) and after (secondary regime) breakaway corrosion. Note that a few alloys exhibit high mass gains also in the absence of K_2CO_3 (see e.g. Fe2.2.5Cr, Fe5Cr3Al and Fe18Cr34Ni in Figure 5.2). These alloys contain insufficient amounts of Cr to form a primary corrosion protection.

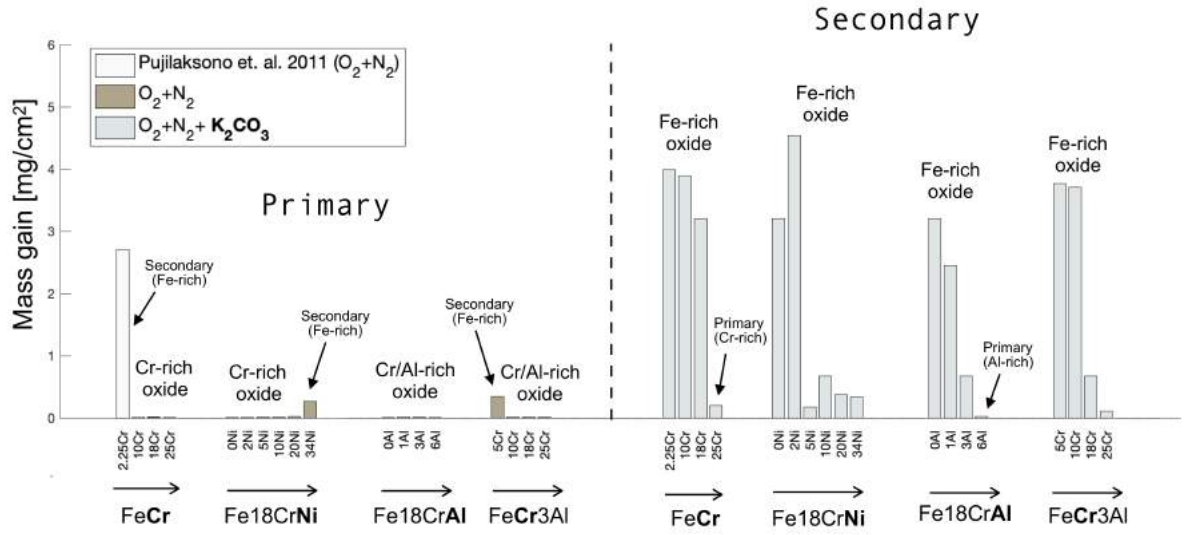

Figure 5.2: a) Mass gains for the FeCr, FeCrNi and FeCrAl model alloys exposed for 24 hours (5% O_2 + 95% N_2) at 600 °C with and without K_2CO_3 deposition prior to exposure. Note that the exposures for the primary corrosion protection (no K_2CO_3) were performed in a regular tube furnace, while the TGA was used to study the secondary corrosion protection (with K_2CO_3), to exclude trends in mass gains caused by different incubation times to breakaway.

The following sections will discuss general aspects of the oxide scales formed on low-alloyed steels, stainless steels, and FeCrAl alloys in the primary and secondary corrosion regimes. Note that stainless steels and FeCrAl alloys can form both a primary and secondary corrosion protection, while the corrosion protection of low-alloyed steels is of only one type (secondary type). It should be noted that the categorisation into different corrosion regimes requires a crude generalisation of the oxide scales. Thus, the properties of the oxides present in each corrosion regime may deviate for other exposure environments, temperatures, and material compositions. However, this section covers only the general aspects of the oxides scales formed in the different corrosion regimes and how the oxidation properties may vary depending on alloy composition.

5.2 Primary corrosion protection

The corrosion protection of stainless steels and FeCrAl alloys exposed in mildly corrosive environments is well known to rely on the formation of a slow-growing, Cr-rich and/or Al-rich corundum type, M_2O_3, oxide scale, i.e. the primary corrosion protection. Low-alloyed steels do not contain sufficient amounts of Cr or Al to form the primary corrosion protection. Thus, low-alloyed steels only form the Fe-rich type of oxide scale (i.e. the secondary type of corrosion protection) [1–3].

The gravimetric results in this work (Figure 5.3) indicate that most of the samples form slow-growing, Cr/Al-rich oxide scales in the mild exposure environment (O_2+N_2), with the exceptions of the low-alloyed model alloys (Fe2.25Cr, Fe5Cr3Al) and the alloy with 34 wt% Ni (Fe18Cr34Ni). These findings are in good agreement with previous studies, and are validated by the plan-view investigation with alloy grains being visible through the oxide scale in the majority of the samples (see Figure 5.4a), indicating thin oxide scales that are typical for the primary corrosion protection. The mass gains remain similar, as compared to the secondary corrosion protection, for the primary corrosion protection formed on all FeCr, FeCrNi and FeCrAl alloys, with calculated oxide scale thicknesses of <100 nm (see Figure 5.3). Small variations in growth rate of the primary corrosion protection could be observed when the amounts of Cr, Ni or Al were altered. However, due to the low mass gains, the observed variations should be treated with caution. More statistics are needed to carry out a thorough investigation of the possible effects. However, this is outside the scope of this thesis.

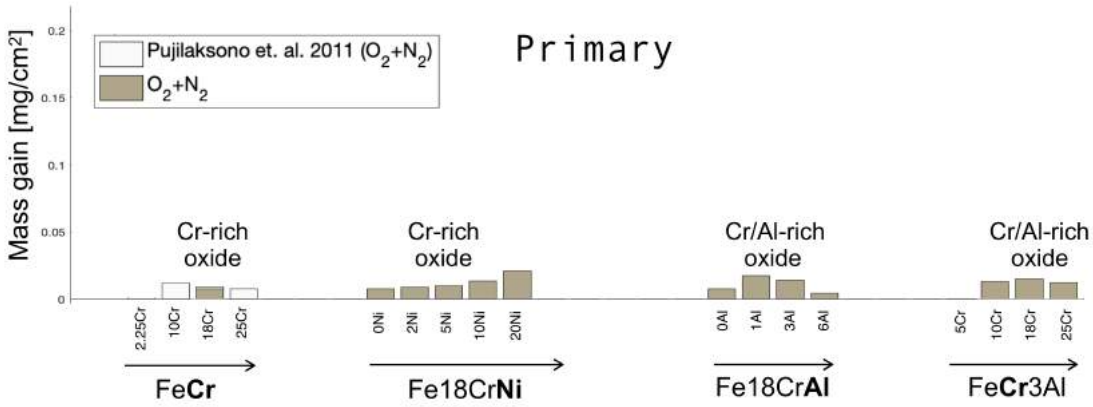

Figure 5.3: Mass gains observed on the FeCr, FeCrNi, and FeCrAl model alloys exposed at 600 °C for 24 hours to a mild environment (5% O_2 + 95% N_2), to study the primary corrosion protection.

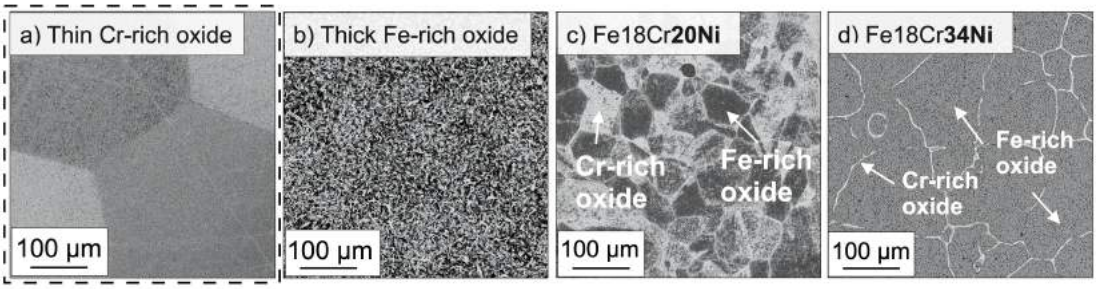

Figure 5.4: Plan-view BSE-SEM images of the types of oxide scales formed after 24 hours of exposure to 5% O_2+ 95% N_2 at 600 °C. The primary corrosion protection (thin Cr/Al-rich oxide) is observed on the majority of the exposed model alloys (a), whereas a thicker, Fe-rich oxide (b) is evident on large areas of the surfaces of the alloys with low Cr content (e.g. Fe2.25Cr [12], Fe5Cr3Al) and on several alloy grains on the Fe18Cr20Ni (c). The Fe18Cr34Ni alloy (d) forms an Fe-rich oxide on the alloy grains and a thinner Cr-rich oxide on top of the alloy grain boundaries.

5.3 Transition from primary to secondary corrosion protection (breakaway corrosion)

Many previous studies have investigated breakaway corrosion and the mechanisms that lead to the breakdown of the primary corrosion protection (see e.g. [4–27, 53, 56]). Although the breakdown mechanisms may vary, depending on exposure conditions, they result in a similar type of transition from a Cr/Al-rich M_2O_3 oxide scale to the formation of a multi-layered, Fe-rich oxide scale [4, 9, 19, 23, 25–27, 37]). Examples of studied breakdown mechanisms are discussed in Section 2.2.3 and often involve the presence of either water vapour, causing Cr-evaporation [6], or alkali, causing the formation of alkali chromates [56].

In this work, the breakdown of the primary corrosion protection is induced by K_2CO_3(s) for all the exposed model alloys, with the aim of promoting Cr-depletion of the oxide (through the formation of potassium chromates), without the influence of other corrosive species (e.g. chlorine). Thus, the method is based on breaking down a Cr-rich M_2O_3. To enable comparisons, the same strategy is used for all the FeCr, FeCrNi, and FeCrAl alloys. As expected, the low-alloyed model alloys (Fe2.25Cr, Fe5Cr3Al), forming Fe-rich oxide scales also in the absence of K_2CO_3, do not break down by this strategy. All the other exposed model alloys exposed, except for the Fe18Cr6Al, break down in the presence of K_2CO_3(s). This observation suggests that the primary corrosion protection of FeCrAl alloys [$(Al,Cr)_2O_3$] act similar to that formed on stainless steels (i.e. the Cr-rich type of oxide scale) at 600 °C for aluminium contents in the range of 0-3 wt%, which is in good agreement with the results from previous studies [37, 46, 47, 70].

As summarised in Table 5.1, the incubation times to breakaway are short (<1 hour) for all exposed alloys, with the exceptions of Fe18Cr and Fe18Cr2Ni (<6 hours), as well as Fe18Cr5Ni ($\sim$ 20 hours). This suggests that the oxide scale thicknesses from the investigation of the secondary corrosion regime (excluding the exceptions) can be used in order

to compare the growth rate of the secondary corrosion protection, without taking into account the incubation times (i.e. that the secondary corrosion protections have grown for different times).

FeCr alloys

Alloy	Incubation time [h]
Fe2.25Cr	<1
Fe10Cr	<1
Fe18Cr	<1
Fe25Cr	-

FeCrNi alloys

Alloy	Incubation time [h]
Fe18Cr	<6
Fe18Cr2Ni	<6
Fe18Cr5Ni	∼20
Fe18Cr10Ni	<1
Fe18Cr20Ni	<1
Fe18Cr34Ni	<1

FeCrAl alloys

Alloy	Incubation time [h]
Fe5Cr3Al	<1
Fe10Cr3Al	<1
Fe18Cr3Al	<1
Fe18Cr1Al	<1
Fe18Cr6Al	-
Fe25Cr3Al	<1

Table 5.1: Approximate incubation times to breakaway for the FeCr, FeCrNi, and FeCrAl model alloys exposed by TGA for 48 hours in the presence of K_2CO_3 (5% O_2 + 95% N_2 at 600 °C). Most of the alloys exhibit very short incubation times, with the exceptions being the Fe18Cr, Fe18Cr2Ni and Fe18Cr5Ni. The oxidation kinetics on a few alloys indicate no breakaway event, so no incubation time is reported for these alloys.

5.4 Secondary corrosion protection

The oxide scale formed after breakaway corrosion, i.e. the secondary corrosion protection, has previously been studied by several groups and is known to consist of a multi-layered, Fe-rich oxide (see e.g. [4, 9, 12, 13, 25–27, 37]). A typical example of the Fe-rich oxide scale formed as the secondary corrosion protection is given in Figure 5.5. The oxide scale consists of an outward-growing iron oxide and an inward-growing mixed spinel. The inward-growing spinel often exhibits a banded microstructure with alternating dense (Region A) and porous (Region B) regions (see Figure 5.5). The banded structure is suggested to be remnants of internal oxidation of type reaction zone (RZ) (i.e. Cr-enriched spinel-type oxide precipitates in a Cr-depleted metal matrix), observed at the scale/metal interface, in agreement with the findings of previous studies [13, 22, 26, 27]. Jonsson et al. [13] concluded that the oxide precipitates were of spinel-type and attributed the RZ to a miscibility gap present in the FeCr spinel at 600 °C. The similarities in microstructure observed between the RZ in this study and those in the previous studies suggest that this structure is formed by a similar mechanism.

This section focuses on the microstructure of the Fe-rich oxide scale formed on the FeCr(Ni/Al) model alloys exposed to 5% O_2 + 95% N_2 at 600 °C, in the presence of K_2CO_3(s). The microstructural changes of the oxides are related to the change in alloy compositions and discussed regarding general aspects of oxidation.

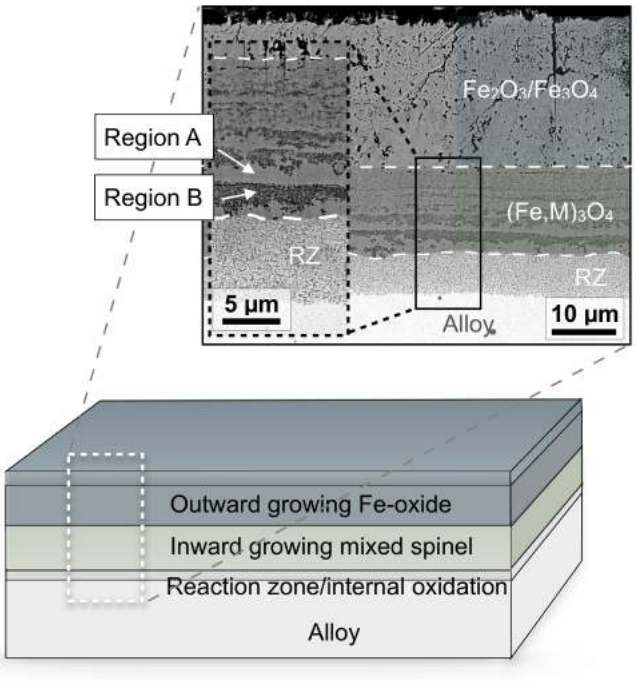

Figure 5.5: Example of the type of oxide scale formed as the secondary corrosion protection on Fe-based alloys at 600 °C. The oxide scale consists of an outward-growing iron oxide (Fe_2O_3/Fe_3O_4) and an inward-growing mixed (Fe,Cr,Al/Ni)-oxide. The inward-growing oxide typically has a banded microstructure with alternating bright (Region A) and dark (Region B) contrast regions and a reaction zone (RZ) at the scale/metal interface.

5.4.1 Low-alloyed steels

Corrosion of low-alloyed steels has previously been studied extensively and are summarised e.g. by Chen and Yuen [48]. The oxide scales formed on low-alloyed steels are multi-layered, consisting of an outward-growing hematite (Fe_2O_3) on top of magnetite (Fe_3O_4) and an inward-growing mixed spinel [$(Fe,Cr,M)_3O_4$] at intermediately high temperatures (<570 °C). While stainless steels and FeCrAl alloys may form both a primary and secondary corrosion protection, the corrosion protection of low-alloyed steels are of only one type (secondary type).

This work investigates the secondary corrosion protection of low-alloyed steels through the oxide scales formed on two model alloys (Fe2.25Cr and Fe5Cr3Al) exposed for 48 hours to 5% O_2 + 95% N_2 at 600 °C, in the presence of K_2CO_3(s). The Fe-rich oxide scales formed on low-alloyed steels are considered important since this material class form a secondary type of corrosion protection also in mild exposure environments. Thus, a detailed microstructural investigation is also conducted of the oxide scale formed on the commercial Fe2.25Cr1Mo steel (see Section 5.5) in the absence and presence of other corrosive species.

Oxide microstructure and composition

The oxide scales formed on the low-alloyed model alloys (Fe2.25Cr, Fe5Cr3Al) are shown in Figure 5.6. The oxide scale thicknesses and microstructures are clearly similar for both alloys. Thus, no great influence of alloying elements are observed on the low-alloyed model alloys. The results from the SEM/EDX analysis are shown in Table 5.2. The oxide scale is composed of an outward-growing, almost pure, Fe-oxide and an inward-growing mixed oxide, depleted from iron and enriched in the other alloying elements.

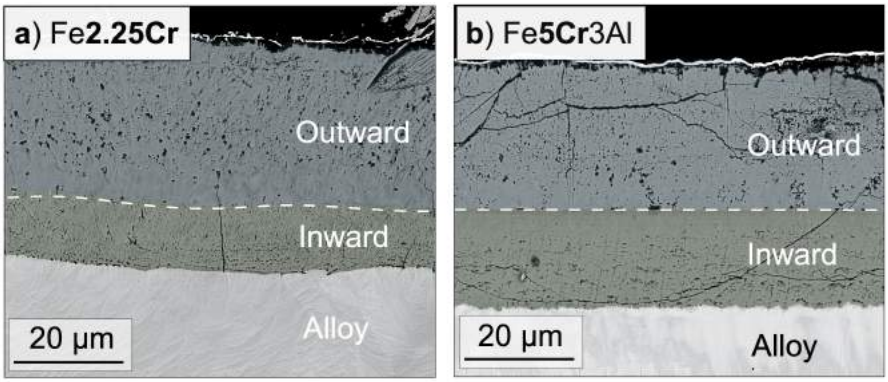

Figure 5.6: BSE-SEM images of the oxide scales formed on the low-alloyed model alloys a) Fe2.25Cr and b) Fe5Cr3Al, after 48 hours of exposure (5% O_2 + 95% N_2, 600 °C) in the presence of K_2CO_3(s). The inward- and outward-growing scales are falsely coloured to allow discrimination and comparison the oxide scales.

It is well known that the diffusivities in the spinel oxide vary for different cations, with the diffusivity of Fe being orders of magnitude higher than those of e.g. Cr and Al [41,42] (see Figure 2.3a). Thus, Cr, Ni, and Al in the spinel can be considered to be immobile in

	Outward growing			Inward growing		
Alloy	Fe	Cr	Al	Fe	Cr	Al
Fe2.25Cr	bal.	<1	-	bal.	6-9 (15 at M/O)	-
Fe5Cr3Al	bal.	<2	<2	bal.	11	16

Table 5.2: Cationic composition (SEM/EDX results in at%) of the outward- and inward-growing scales formed on two low-alloyed model alloys (Fe2.25Cr, Fe5Cr3Al) exposed for 48 hours at 600 °C in 5%O_2 + 95% N_2.

relation to Fe, resulting in an Fe-depleted spinel oxide, as the Fe diffuses outwards. Thus, the distributions of cations (sharp interface) observed in this study, in combination with previous studies, and the correspondence with thermodynamic expectations (see Ellingham diagram in 2.1), strongly suggest that the inward-growing oxide is of spinel type, and that the growth of the total oxide scale is diffusion-controlled. The Fe-depletion of the inward-growing spinel is in good agreement with the results reported in previous studies (see e.g. [10, 12, 13]) and can be regarded as a relative enrichment of other alloying elements. Therefore, during the time that the outward-growing scale is growing, the composition of the inward-growing spinel cannot be treated as constant, and only trends in changes in the chemical composition are considered relevant for the overall understanding.

The measured oxide scale thicknesses are summarised in Table 5.3, along with the relative amounts of inward- and outward-growing scales and the measured oxide grain sizes. The measured thicknesses and relative amounts, are in good agreement with data presented in previous studies [12, 71]) as well as the estimated thicknesses, calculated from the mass gain data in this study. The relative amounts of inward- and outward-growing scales vary slightly for the different alloys (see Table 5.3). It may be noted that the thicker oxides have a larger proportion of inward-growing scale, possibly indicating a correlation between enhanced anion diffusion (inward growth) and higher oxide growth rates for low-alloyed steels at the temperature range studied. However, since the variation is small, more statistics are needed to validate the trend and draw any firm conclusions.

Alloy	Thickness [µm]	Out [µm]	In [µm]	Out:In [-]	Grain size Out [nm]	Grain size In [nm]
Fe2.25Cr	41	29	12	70:30	700 (500-900)	100-500
Fe5Cr3Al	50	29	21	58:42	-	-
Fe2.25Cr1Mo **(24h)***	0.5	0.4	0.1	80:20	M:140 (H:75)	-

*Table 5.3: Oxide scale thicknesses, relative amounts of inward- and outward-growing scales and oxide grain sizes of the examined oxides formed on Fe2.25Cr and Fe5Cr3Al exposed for 48 hours at 600 °C in the presence of K_2CO_3(s). The grains measured in the outward-growing scale are assumed to be magnetite grains. *The commercial alloy Fe2.25Cr1Mo is included for comparative purposes, including magnetite(M) and hematite (H), even though exposed under different conditions (5% O_2 + 20% H_2O + 75% N_2, 400 °C, 24 hours).*

5.4.2 Stainless steels

The oxide scales formed after breakaway corrosion of stainless steels is known to have similar features to the scales formed on low-alloyed steels [4, 9, 12, 13, 25, 26]. However, their microstructure and protective properties are not identical [13, 25]. In this work, the secondary corrosion protection of stainless steels is studied on FeCr(Ni) model alloys with varying amounts of Cr or Ni, exposed for 48 hours to 5% O_2 + 95% N_2 at 600 °C, in the presence of K_2CO_3(s), (see Table 3.1). Changes in oxide microstructure and general oxidation properties are studied in order to increase the understanding of how the secondary corrosion regime may vary for different materials.

Oxide microstructure and composition

The oxide scales formed on a few selected FeCr and FeCrNi model alloys are shown in Figures 5.7 (varying Cr) and 5.8 (varying Ni), representing the secondary corrosion regime of stainless steels. The low-alloyed Fe2.25Cr is included for comparative purposes. It is evident that the oxide scale thicknesses (i.e. growth rates) of the secondary corrosion protection do not vary significantly for the FeCr model alloys as the amount of Cr is increased from 2.25 wt% to 18 wt% Cr (see Figure 5.7). However, the growth rate of the secondary corrosion protection formed on the FeCrNi model alloys is observed to be greatly influenced as the alloy composition is altered. Possible explanations for these effects are discussed below and greater in detail in **Paper II**. The growth rate of the secondary corrosion protection formed on the FeCrNi model alloys decrease rapidly when 5 wt% Ni is reached, whereas it remains almost constant as the level of Ni is further increased (5-34 wt% Ni). Note that the FeCrNi system contains alloys with different crystal structures (BCC/FCC; see Table 3.1). This could be one of the explanations to the observed effect Ni (between 2-10 wt% Ni) on the secondary corrosion protection, which needs to be studied in greater detail before firm conclusions can be drawn. Note that the growth kinetics observed on the Fe25Cr alloy indicates that this alloy remains in the primary corrosion regime. Therefore, this oxide is not considered in the analysis of the secondary corrosion protection.

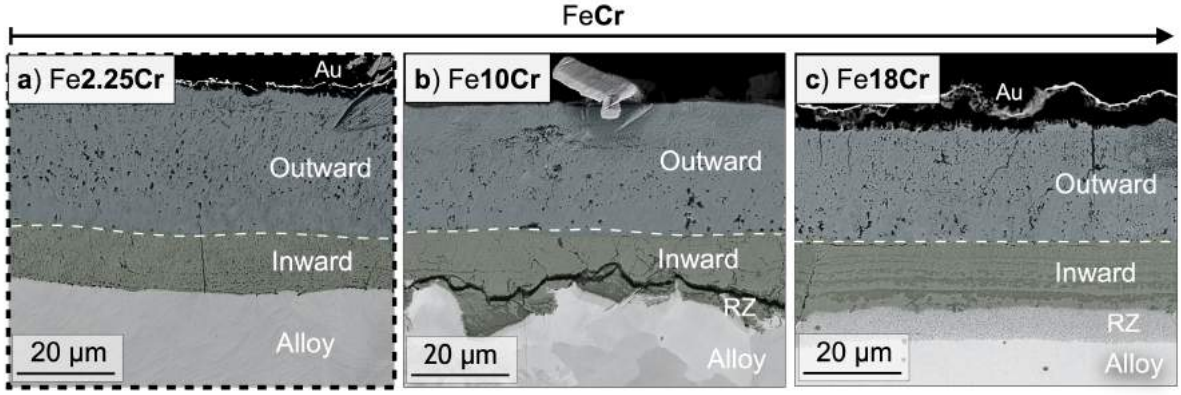

Figure 5.7: BSE-SEM images of the oxide scales formed on a selection of FeCr model alloys representing stainless steels with varying amounts of Cr, after 48 hours of exposure (5% O_2 + 95% N_2 + 1 mg K_2CO_3(s) at 600 °C). The inward- and outward-growing scales are falsely coloured to allow discrimination and comparison of the oxide scales.

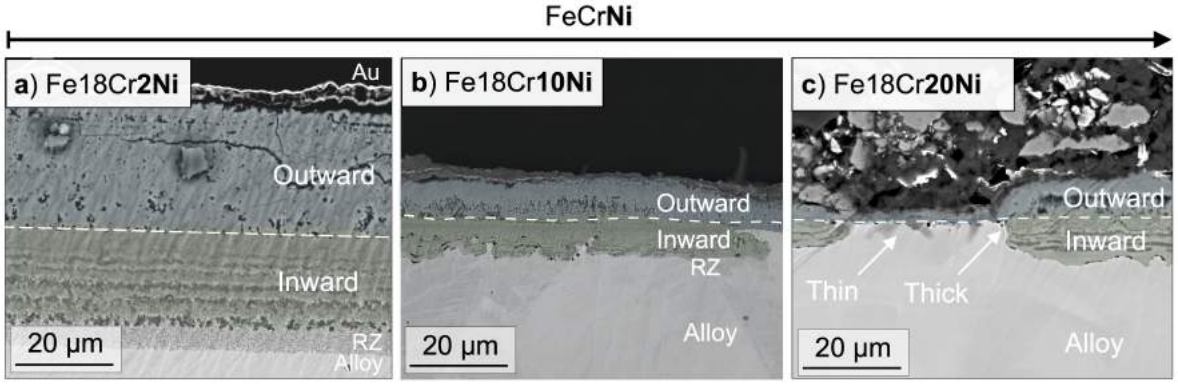

Figure 5.8: BSE-SEM images of the oxide scales formed on a selection of FeCrNi model alloys representing stainless steels with varying amounts of Ni, after 48 hours of exposure (5% O_2 + 95% N_2 + 1 mg K_2CO_3(s) at 600 °C). The inward- and outward-growing scales are falsely coloured to allow discrimination and comparison of the oxide scales. Note that the alloy containing 20 wt% Ni (Fe18Cr20Ni) grow less homogeneous and contain both thin and thicker oxide regions (c).

Regardless of the oxide growth rates, the oxide scale formed on all the exposed FeCr(Ni) alloys in the secondary corrosion regime, are composed of multi-layered, Fe-rich oxide scales, with similar features as the low-alloyed steels. All alloying elements, apart from Fe and small amounts (<2%) of Cr, remain in the Fe-depleted inward-growing spinel, while the outward-growing scale is composed of almost pure iron oxide (see Table 5.4), which is in good agreement with the results from previous studies [10, 12, 13]. However, the microstructures of the inward-growing spinels formed on the stainless model alloys, have a more prominent porous and banded structure, as compared to the low-alloyed steels (see the alternating Regions A and B in Figure 5.5).

The overall composition of the inward-growing spinel changes as the alloying elements are varied (see Table 5.4). The maximum amounts of Cr and Ni observed are below the maximum amount of trivalent (Cr≤67.7 at%) and divalent (Ni ≤33.3 at%) ions for all the exposed model alloys, with the exception of the Fe18Cr20Ni alloy, which contains higher levels of Ni. Note that the Fe18Cr34Ni alloy was not analysed in cross-section due to issues associated with sample preparation. It should be noted that the SEM/EDX analysis result in a composition from a relatively large volume (∼1 µm at 20 keV). Thus, the larger amounts of Ni detected in the inward-growing oxide may reflect a mixture of e.g. Ni-rich spinel and NiO. Further studies are underway to better quantify the local composition of the inward-growing oxides using tools for chemical analysis with higher spatial resolution (STEM/EDX).

The periodic microstructure (Regions A and B) alternates with a frequency that decreases closer to the alloy interface. The relative amounts of porous Region B are difficult to quantify but are in the range of 30-40 % of the inward-growing scale. Regarding the composition of the inward-growing scale, the alternations and the porous structure makes SEM/EDX quantification difficult, partly because the interaction volume of the EDX-

	Outward-growing			Inward-growing		
Alloy	Fe	Cr	Ni	Fe	Cr	Ni
Fe2.25Cr	bal.	<1	-	bal.	6-9 (15 at M/O interface)	-
Fe10Cr	bal.	<1	-	bal.	25-30	-
Fe18Cr	bal.	<2	-	bal.	43 (A:39-41, B:45-48)*	-
Fe25Cr	-	-	-	-	-	-
Fe18Cr(0Ni)	bal.	<2	-	bal.	43 (A:39-41, B:45-48)*	-
Fe18Cr2Ni	bal.	<2	0	bal.	(A:37-39, B:46)*	2-3
Fe18Cr5Ni	bal.	<2	0	bal.	44-46	4-6
Fe18Cr10Ni	bal.	<2	0	bal.	35-38	8-18
Fe18Cr20Ni	bal.	<1	0	bal.	(A:29-30, B:44-45)*	(A:39-42, B:17-19)*

*Table 5.4: Cationic composition (SEM/EDX results in at%) of the outward and inward-growing scale formed on FeCr(Ni) model alloys exposed for 48 hours at 600 °C to 5%O_2 + 95% N_2. The inward-growing scale comprises two types of regions (Region A and Region B; see Figure 5.5). *Data is acquired from the centre of Region A and Region B, respectively. Note that the interaction volume is expected to partly cover both regions.*

analysis is expected to partly cover both regions. However, the results from the SEM/EDX analysis (see Table 5.4) strongly indicate that the composition alternates between Region A and Region B. The porous regions (Region B) are enriched in Cr, as compared to the dense Region A, suggested to be attributed to a higher Fe-depletion from these regions. Thus, the variation in composition between Region A and B generates an alternating concentration gradient throughout the spinel. If one regards the concentration gradient as a driving force for ionic diffusion, the ionic flux through the inward-growing spinel, would also be expected to change periodically throughout the spinel. Thus, the complex microstructure and changing chemical composition of the inward-growing spinel requires a thorough microstructural investigation with higher spatial resolution to better quantify the composition of each region.

The measured thicknesses, relative amounts of inward- and outward-growing scales, as well as measured oxide grain sizes are summarised in Table 5.5. The amounts of inward- and outward-growing scales do not change significantly as the alloy composition (or alloy microstructure) is changed within each set of alloys (FeCr and FeCrNi). The relative amounts remain in the range of 30-40% inward-growing and 60-70% outward-growing for the FeCr alloys, and 40-50% inward-growing and 50-60% outward-growing for the FeCrNi alloys. This indicates that the diffusion of anions (oxygen) and cations (Fe) are affected to similar extents as the alloy composition is altered. However, it should be borne in mind that an enhanced diffusion in one direction could alter the diffusion properties in the other direction. Further studies are underway to evaluate how the diffusivities of oxygen and other cations are influenced by an altered composition of the spinel.

Another important factor that influences ionic diffusion through the scale are short circuit diffusion paths, such as grain boundaries. An example, showing the oxide grains of the outward-growing oxide, can be seen in Figure 5.9 and the grain sizes are summarised in Table 5.5. It is evident that the oxide grains in the outward-growing scale are larger for

the thick and fast-growing oxide scale formed on Fe18Cr2Ni (Figure 5.9a) as compared to the thinner oxide formed on Fe18Cr10Ni (Figure 5.9b). The same trend is observed for the inward-growing scale, even though this scale was more difficult to image due to its porous microstructure and smaller grain sizes.

Alloy	Thickness [µm]	Out [µm]	In [µm]	Out:In [-]	Grain size Out [nm]	Grain size In [nm]
Fe2.25Cr	41	29	12	70:30	700(500-900)	500(100-500)
Fe10Cr	37	26	11	70:30	750	250
Fe18Cr	37	23	14	62:38	1000	-
Fe25Cr	-	-	-	-	-	-
Fe18Cr(0Ni)	37	23	14	62:38	1000	-
Fe18Cr2Ni	45	26	19	58:42	1000	-
Fe18Cr5Ni	28	17	11	61:39	200	300
Fe18Cr10Ni	17	9	8	53:47	150	100
Fe18Cr20Ni	16	8	8	50:50	200	-
Fe18Cr34Ni	-	-	-	-	-	-

Table 5.5: Measured oxide scale thicknesses, relative amounts of inward- and outward-growing scales and oxide grain sizes of the examined secondary corrosion protection formed on the FeCr(Ni) model alloys with varying amounts of Cr or Ni exposed for 48 hours at 600 °C. Note that the oxide scale formed on the Fe18Cr34Ni alloy was not examined in cross-section. Most samples showed no visible contrast between hematite and magnetite. Thus, it is assumed that the grains measured in the outward-growing scale are magnetite grains.

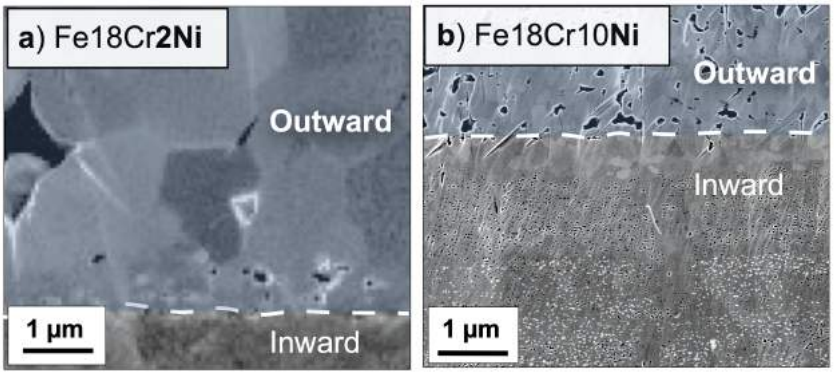

Figure 5.9: Ion-induced SE (a) and low-keV BSE (b) images showing the oxide grains of the outward-growing oxides formed on: a) a fast-growing and b) a slow-growing oxide scale after 48 hours of exposure at 600 °C in the presence of K_2CO_3 (5% O_2 + 95% N_2). The grain sizes are larger in the thicker oxide scale, as compared to the thinner oxide scale.

5.4.3 FeCrAl alloys

Previous studies on the secondary corrosion protection of FeCrAl alloys at 600 °C are scarce. However, a few studies have been performed in oxidising atmospheres in the presence of KCl(s), as well as H_2O(g) (see e.g. [37, 58, 59]). The present work focuses on

investigating the secondary corrosion protection of FeCrAl alloys through model alloys with varying amounts of Cr or Al, exposed for 48 hours to 5% O_2 + 95% N_2 at 600 °C, in the presence of K_2CO_3(s), (see Table 3.1).

Oxide microstructure and composition

The oxide scales formed on the FeCrAl model alloys after 48 hours in the secondary corrosion regime are shown in Figures 5.10 (varying Al) and 5.11 (varying Cr), including the Fe18Cr for comparative purposes and a better insights into the influences of alloying elements. The measured thicknesses (see Table 5.7) are in good agreement with the calculated thicknesses based on mass gain data. The oxide scale thicknesses (i.e. growth rates) are greatly reduced as the alloy composition is altered, both with respect to increased amounts of Al and Cr (see Figures 5.10 and 5.11). The reduction in thickness is close to linear as the amount of Al is increased from 0-3 wt%, while a sudden drop is observed as the amount of Cr is increased from 10 to 18 wt%. There are no considerable differences in the growth rates within the ranges of 5-10 wt% Cr or 18-25 wt% Cr. Possible explanations for these effects are discussed below and in greater detail in **Paper II**. Note that the alloy with 6 wt% Al (Fe18Cr6Al) remains in the primary corrosion regime, exhibiting a mass gain corresponding to a calculated thickness of <100 nm.

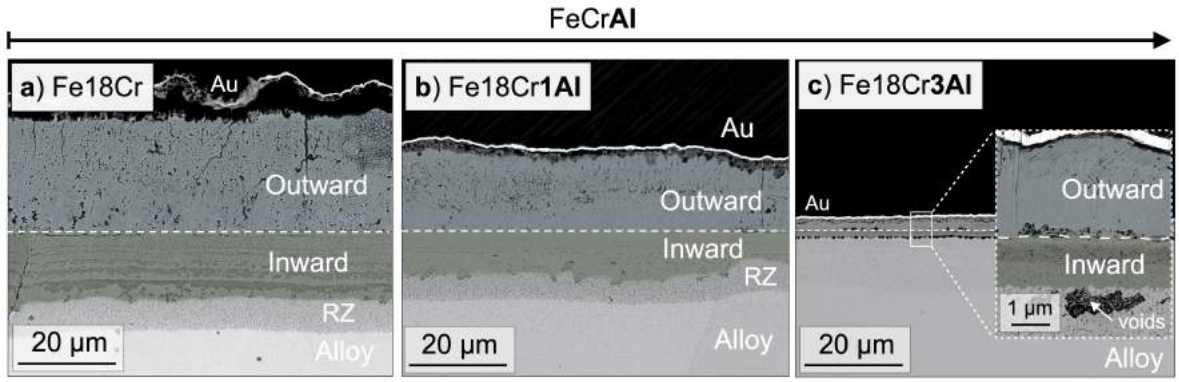

Figure 5.10: BSE-SEM images of the oxide scales formed on a selection of FeCr(Al) model alloys with varying amounts of Al, after 48 hours of exposure (5% O_2 + 95% N_2 + 1 mg K_2CO_3(s) at 600 °C). The inward and outward-growing scales are falsely coloured to better distinguish and compare the oxide scales.

All the oxide scales formed on the FeCrAl alloys in the secondary corrosion regime are multi-layered, Fe-rich oxide scales, with a microstructure similar to the secondary corrosion protection of stainless steels and low-alloyed steels. As shown in Table 5.6, all the alloying elements remain in the Fe-depleted, inward-growing spinel while the outward-growing scale is composed of almost pure iron oxide, in good agreement with previous studies (see e.g. [37]). The porous and banded microstructure (see Region A and B in Figure 5.5) observed in the inward-growing spinel on the stainless model alloys is also prominent on the FeCrAl alloys (see Figures 5.10-5.11). However, the FeCrAl alloys with high Cr contents (Fe18Cr3Al, Fe25Cr3Al), which form thinner oxide scales (<5 µm after 48 hours), only show initial indications of this structure. Longer exposure times would be needed to determine whether the periodic, banded structure appears as the oxides grow

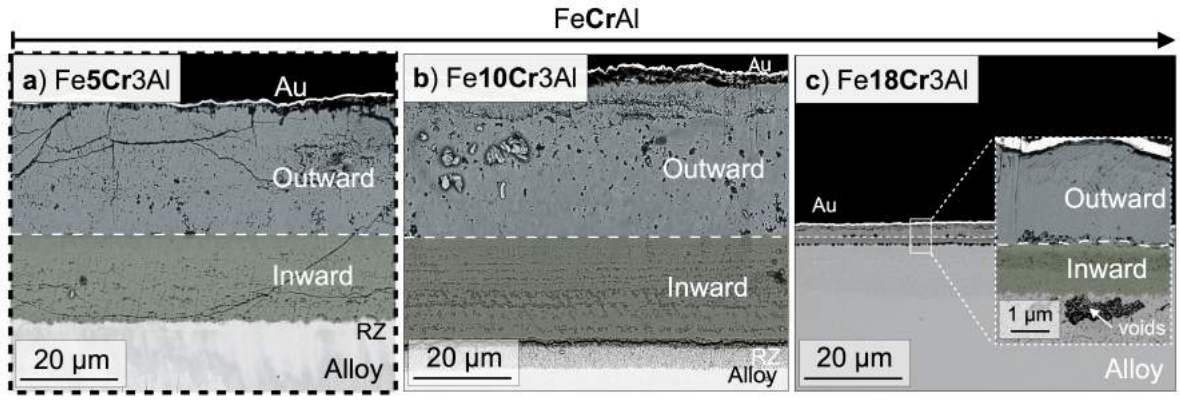

Figure 5.11: BSE-SEM images of the oxide scales formed on a selection of FeCrAl model alloys with varying amounts of Cr, after 48 hours of exposure (5% O_2 + 95% N_2 + 1 mg K_2CO_3(s) at 600 °C). The inward and outward-growing scales are falsely coloured to better distinguish and compare the oxide scales.

thicker. These two alloys also show indications of nitridation in the alloy and the presence of Al-rich voids at the scale/metal interface (see Figure 5.11c).

The SEM/EDX analysis of the inward-growing spinel indicates enrichment of Cr in the porous Region B (see Table 5.6), while the amounts of Al remain almost constant throughout the spinel. However, the SEM/EDX quantification of the inward-growing scale is difficult on the thinner oxide scales, due to the interaction volume, which is expected to cover also the alloy beneath the oxide scale. The compositions of the inward-growing spinels in FeCrAl alloys are considered important from a mechanistic perspective, given that Al is trivalent and would be expected to compete for the same sites as Cr^{3+}. However, the porous structure and low spatial resolution of SEM/EDX limits the possibility to perform accurate quantification of each region. Further studies are ongoing (STEM/EDX) to define the compositions of the spinels formed on FeCrAl alloys in further detail.

	Outward growing			Inward growing		
Alloy	Fe	Cr	Al	Fe	Cr	Al
Fe18Cr(0Al)	bal.	<2	-	bal.	43 (A:39-41, B:45-48)*	-
Fe18Cr1Al	bal.	<2	<1	bal.	39	5-6
Fe18Cr3Al**	bal.	4-9	1-3	bal.	(A: 29-32, B: 50-51)*	11-13
Fe5Cr3Al	bal.	-	-	bal.	-	-
Fe10Cr3Al	bal.	<1	<1	bal.	20-22	14-15
Fe18Cr3Al**	bal.	4-9	1-3	bal.	(A: 29-32, B: 50-51)*	11-13
Fe25Cr3Al**	bal.	23-29	1-2	bal.	55-59	13-14

*Table 5.6: Cationic composition (SEM/EDX results in at%) of the outward and inward-growing scale formed on FeCrAl model alloys exposed for 48 hours at 600 °C in 5% O_2 + 95% N_2. Note that the inward-growing scale is composed of two types of regions (Region A and B, see Figure 5.5). Note that the interaction volume for the acquired data in * is expected to partly cover both Region A and B, as well as ** the alloy beneath the oxide scale.*

The oxide scale thicknesses, relative amounts of inward- and outward-growing scales, as well as oxide grain sizes measured are summarised in Table 5.7. The relative amounts of inward- and outward-growing scales remain similar for all FeCrAl alloys (approximately 40% inward- and 60% outward-growing). As previously discussed, this indicates that anion and cation diffusion in the secondary corrosion protection are affected to similar extents as the alloy composition is altered, in similarity to the secondary corrosion protection of stainless steels. However, a slightly higher amount of inward-growing scale is observed on the alloys with high Cr-content (Fe18Cr3Al, Fe25Cr3Al), that also have formed thinner oxide scales. Thus, it is tempting to speculate that the reduced amount of inward anion diffusion observed is correlated to a reduction in growth rate. However, the fast-growing oxide scales grown on the low-alloyed steels also showed reduced amount of inward-growing scale (see Table 5.3), contradicting this speculation.

Alloy	Thickness [µm]	Out [µm]	In [µm]	Out:In [%:%]	Grain size Out [nm]	Grain size In [nm]
Fe18Cr(0Al), **24 h**	20	12	8	60:40	450	-
Fe18Cr1Al, **24 h**	16	10	6	62:38	275	-
Fe18Cr3Al, **24 h**	3	2	1	60:40	200	-
Fe18Cr(0Al)	37	23	14	62:38	1000	-
Fe18Cr1Al	30	18	12	60:40	-	-
Fe18Cr3Al	4	2.5	1.5	62:38	-	-
Fe5Cr3Al	50	29	21	58:42	-	-
Fe10Cr3Al	52	30	22	58:42	850	-
Fe18Cr3Al	4	2.5	1.5	62:38	-	-
Fe25Cr3Al	3.5	2.5	1	71:29	-	-

Table 5.7: Oxide scale thicknesses, relative amounts of inward- and outward-growing scales and oxide grain sizes of the examined secondary corrosion protection formed on the FeCr(Al) model alloys with varying amounts of Cr or Al. Note that some of the oxide scales studied were exposed for 24 hours in a regular tube furnace. Most samples showed no visible contrast between hematite and magnetite. Therefore, it is assumed that hematite is thin and that the grains measured in the outward-growing scale are magnetite grains.

Figure 5.12 shows an example of the oxide grains of the outward-growing oxide scales formed on Fe18CrxAl (x=0,1,3 wt%) after 24 hours of exposure. As summarised in Table 5.7, smaller grains are observed on the slower-growing oxide scales, in similarity to the observations on the FeCr(Ni) model alloys. Note that the grains of the inward-growing scales were not successfully imaged in these cross-sections.

Grain boundary diffusion is normally associated with faster ionic diffusion at intermediately high temperatures, due to lower activation energies. Thus, smaller oxide grains, i.e. more oxide grain boundaries, would be expected to result in faster diffusion of charged species through the scale, and consequently thicker oxide scales. Interestingly, the microstructural investigation performed in this work indicates the opposite, both for low-alloyed steels, stainless steels, and FeCrAl alloys (see Figure 5.13a). These observations could be an indication of either that grain boundary diffusion is not rate-limiting for the

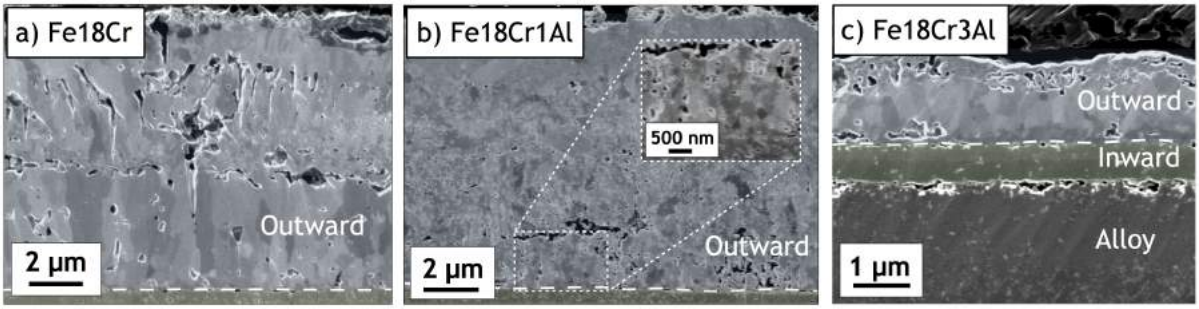

Figure 5.12: Ion-induced SE images showing the oxide grains of the outward-growing oxides formed on Fe18CrxAl (x=0,1,3) model alloys with varying amounts of Al after 24 hours of exposure at 600 °C in the presence of K_2CO_3 (5% O_2 + 95% N_2). The grain sizes are larger in the thicker oxide scale (a), as compared to the thinner (b).

growth of the secondary corrosion protection under the given exposure conditions, or that the diffusion rates along grain boundaries are reduced in the slow-growing oxide scales. Further studies are needed to conclude these indications, since grain growth must also be considered before the number of grain boundaries (i.e. grain size) can be truly correlated to the amount of grain boundary diffusion. The grain growth of the middle magnetite layer was briefly studied on the Fe18Cr model alloy showing considerable grain growth up to 48 hours of exposure (see Figure 5.13b). Thus, the trend towards larger grains with higher mass gains should only be taken as an indication as to how grain boundary diffusion in magnetite can influence the total growth rate of the Fe-rich oxide scale.

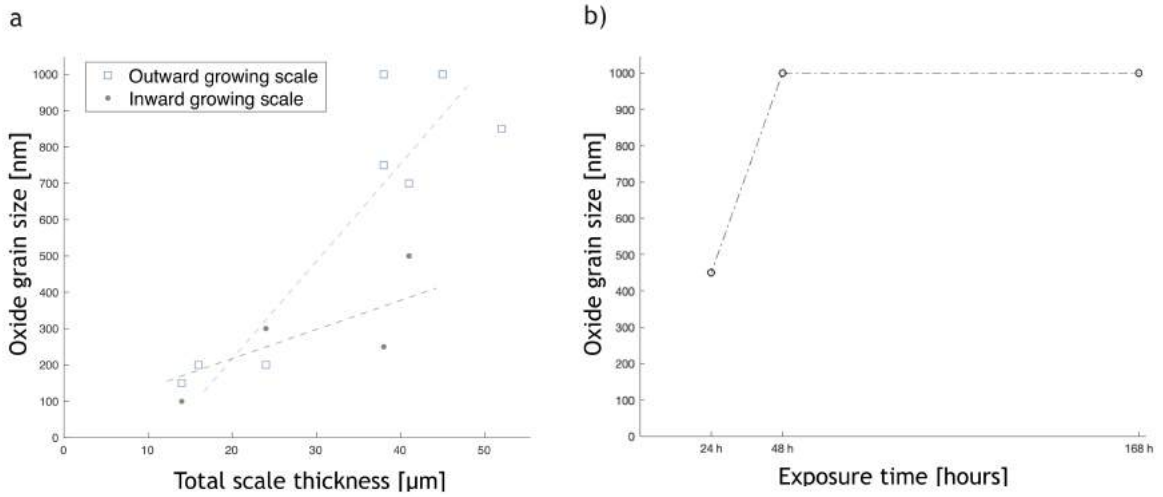

Figure 5.13: Grain size of the: a) inward- and outward-growing oxides as a function of the total oxide scale thickness for several FeCr(Ni/Al) model alloys exposed for 48 hours, and b) the outward-growing oxide formed on Fe18Cr exposed in the presence of K_2CO_3 (5% O_2 + 95% N_2 at 600 °C). The trend-lines in a) show that the grain sizes are larger on the thicker oxide scales, while b) shows that grain growth is evident up to 48 hours in the outward-growing oxide formed on Fe18Cr.

5.5 Influences of corrosive species on the secondary corrosion protection

Chlorine- and alkali-containing species are known to accelerated the corrosion of Fe-based alloys, including low-alloyed steels [29, 71–83], stainless steels and FeCrAl alloys [18–21, 26, 27, 29, 37, 56–59, 74–77, 79, 80, 84–89]. The proposed corrosion mechanisms are numerous and are typically focused on: a) how these species induce breakdown of the primary corrosion protection; or b) how the presence of chlorine-containing species accelerates the corrosion process through chemical reactions, such as, for example, the proposed active oxidation mechanism [55, 74], where chlorine gas forms metal chlorides that transform into porous oxides. The mechanisms of the accelerated corrosion caused by these species are not the scope of this thesis. However, the influences of alkali and chlorine are discussed briefly regarding how its presence may change the microstructure of the Fe-rich oxide scale, as to better understand how it may change the capability of the Fe-rich oxide to withstand further corrosion caused by these species.

Since the oxide scale formed on low-alloyed steels are of only one type (secondary type), its properties in various environments may be used to increase our understanding as to how corrosive species may affect the secondary corrosion protection also on stainless steels and FeCrAl alloys. Thus, in this work, the influence of exposure environment on the microstructure of the Fe-rich oxide scale is investigated on the low-alloyed steel Fe2.25Cr1Mo, exposed for 24 hours to 5% O_2 + 20% H_2O + N_2(bal.) at 400 °C in the presence of different alkali- and chlorine-containing species (HCl(g), HCl(g)+KCl(s), and KCl(s)). Further studies on how different alloy compositions of stainless steels and FeCrAl alloys may change the capacity to withstand these corrosive species are planned to be conducted in the future.

5.5.1 Gravimetry

The results of the thermogravimetric analysis are shown in Figure 5.14, including a reference sample exposed to 5% O_2 + 20% H_2O + N_2(bal.) in the absence of chlorine. The mass gains are in good agreement with the values reported in previous studies conducted under similar exposure conditions [71,82]. It is evident that some corrosive species changes the kinetics, in particular in the presence of KCl(s). However, not all of the mass gain curves are necessarily assigned to oxidation, but can be caused by additional reactions (see below). As an example, the kinetics of the combined HCl(g)+KCl(s) exposure is very different from the kinetics of either the HCl(g)-only or the KCl(s)-only exposure. Larsson et al. [83] suggested the kinetics for these exposure conditions to be influenced by the formation of a continuous layer of metal chlorides underneath the KCl(s) deposited particles, acting as an electronic insulator. Nevertheless, the microstructural investigation performed in this work (see below), shows that the growth of the base oxide (in between the KCl(s)) particles is not affected as dramatically. The oxidation kinetics are also drastically changed as the steel is exposed in the presence of KCl(s)-only (without HCl). The growth is interrupted after approximately 12 hours (see kinetic transition in Figure 5.14). The kinetic transition is attributed to scale cracking and delamination of the oxide scale (for detailed rationale, see **Paper I**). The oxidation kinetics is parabolic, in similarity to

the reference exposure, although with a parabolic rate constant approximately 10 times higher than that of the reference sample. The oxidation kinetics remain parabolic, with similar rate constants, before and after the kinetic transitions. Thus, both the reference exposure, HCl(g) exposure and KCl(s) exposure result in nearly parabolic kinetics, indicating diffusion-controlled growth, albeit with different parabolic rate constants.

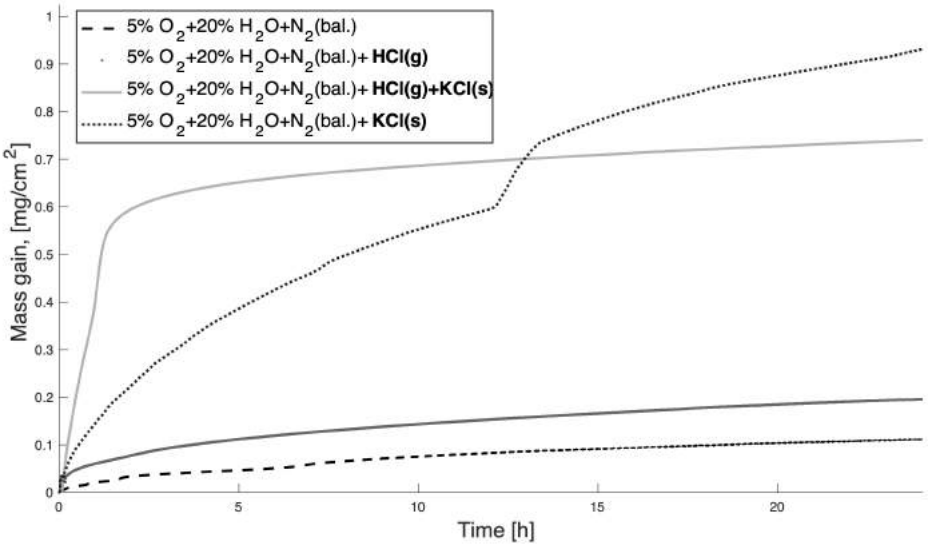

Figure 5.14: TGA results for Fe2.25Cr1Mo exposed to 5% O_2 + 20% H_2O + N_2(bal.) for 24 hours at 400 °C in the presence of HCl(g) and/or KCl(s). The TGA exposures and preparation were performed by Dr. Erik Larsson.

5.5.2 Oxide microstructure and composition

The oxide scale thicknesses and relative amounts of outward- and inward-growing scales formed in the different environments are summarised in Table 5.8. It is obvious that the presence of different chlorine containing species affect the growth rate of the Fe-rich oxide scale and that the relative amounts of inward- and outward-growing scales changes as the environment is altered (see below). The oxides were analysed in detail by STEM/EDX, as shown in Figure 5.15-5.18).

Exposure	Thickness [μm]	Out:In [%:%]
Ref. [5% O_2 + 20% H_2O + N_2(bal.)]	0.5	80:20
Ref. + HCl(g)	1.3	77:23
Ref. + KCl(s) (upper sub-scale)	6-8	70:30
Ref. + KCl(s) (lower sub-scale)	6-8	55:45
Ref. + KCl(s) + HCl(g)	3.3	45-50:50-55

Table 5.8: Summary of the measured oxide scale thicknesses and relative amounts of inward- and outward-growing scales for the secondary corrosion protection formed on the commercial low-alloyed steel (Fe2.25Cr1Mo) exposed for 24 hours at 400 °C (5% O_2 + 20% H_2O + N_2(bal.)) in the presence and absence of different chlorine- and alkali-containing species.

Reference exposure (O_2+H_2O+N_2 at 400 °C)

The oxide scale formed in reference exposure (5% O_2 + 20% H_2O + 75% N_2 at 400 °C, no chlorine) is shown in Figure 5.15. The oxide scale is multi-layered and composed of outward-growing hematite (Fe_2O_3) on top of magnetite (Fe_3O_4) and an inward-growing mixed (Fe,Cr,M) spinel, which is in good agreement with the low alloyed model alloys investigated in this work, as well as findings of previous studies of low-alloyed steels and iron [12,20,48,77,81,90,91]. The results from the STEM/EDX are shown in Figure 5.15b. The outward-growing oxide is composed of almost pure iron oxide, while all alloying elements remain in the Fe-depleted, inward-growing oxide, containing an average of 10 at%Cr (6.5-19 at%), 2 at% Si (1-4 at%), 1-2 at% Mo, with iron in balance (excluding oxygen from the quantification). The STEM/EDX analysis of the inward-growing spinel indicates that the distribution of Cr is inhomogeneous (see line-scan of Cr in Figure 5.15), ranging form 6.5-19 at% (cation). Inhomogeneous distributions of alloying elements may affect both lattice and short-circuit diffusion through the spinel. Thus, this needs to be considered when developing models for growth of the secondary corrosion protection, as well as when seeking to develop ways to improve its protective properties.

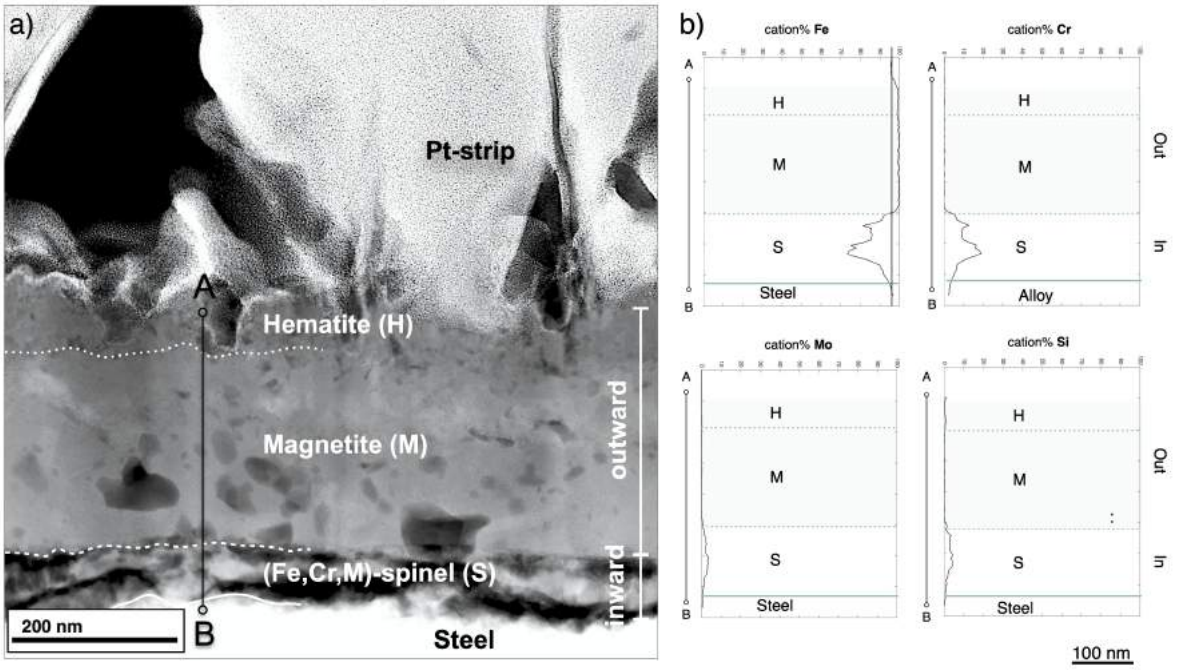

Figure 5.15: STEM/EDX analysis of the oxide scale formed on Fe-2.25Cr-1Mo steel exposed in reference conditions (5% O_2 + 20% H_2O + 75% N_2) for 24 hours at 400 °C. a) HAADF-STEM image marking the position of the STEM/EDX line scans in b) (see A-B). The STEM/EDX analysis shows that the scale is layered, with Cr being present only in the inward-growing oxide. The distribution of Cr (b) in the inward-growing oxide is inhomogeneous and ranges from 6.5-19 at% (cations). The TEM was operated by Dr. Mohammad Sattari.

Influence of HCl(g)

Figure 5.16 shows that the presence of HCl(g) increases the final oxide thickness (i.e. growth rate), as compared to the reference exposure. The oxide scale thickness is approximately 1.3 µm, which is in good agreement with the calculated thicknesses based on mass gain data (see Figure 5.16). Even though the oxide scale is thicker than that of the reference sample, the microstructure is very similar, exhibiting a multi-layered scale with a similar ratio of outward-growing (Fe_2O_3/Fe_3O_4) and inward-growing [$(Fe,Cr,M)_3O_4$] scales (75-80:20-25) (see Table 5.8).

The STEM/EDX analysis (see Figure 5.16b) shows that all the alloying elements, except for iron, remain in the spinel, in similarity to the reference exposure. No chlorine, or indications thereof, is detected in the oxide scale either by either SEM/EDX or STEM/EDX. However, trace amounts of chlorine (below the detection limit of STEM/EDX) may still be present. Other analytical tools with lower detection limits, such as APT, are needed to determine conclusively if chlorine is at all present in the oxide scale. The increase in growth rate, together with the absence of chlorine in the scale, suggests that chlorine plays a more modest role than e.g. that proposed by the active oxidation process [55, 74]. The catalytic role of chlorine in the active oxidation process would predict the amount of outward-growing scale to increase as the metal chlorides would evaporate and transform into porous oxides. Thus, the results from this work, showing a similar increase in both the inward- and outward-growing scales, may also be an indication of that the active oxidation process is not the main mechanism underlying the accelerated growth observed under these conditions.

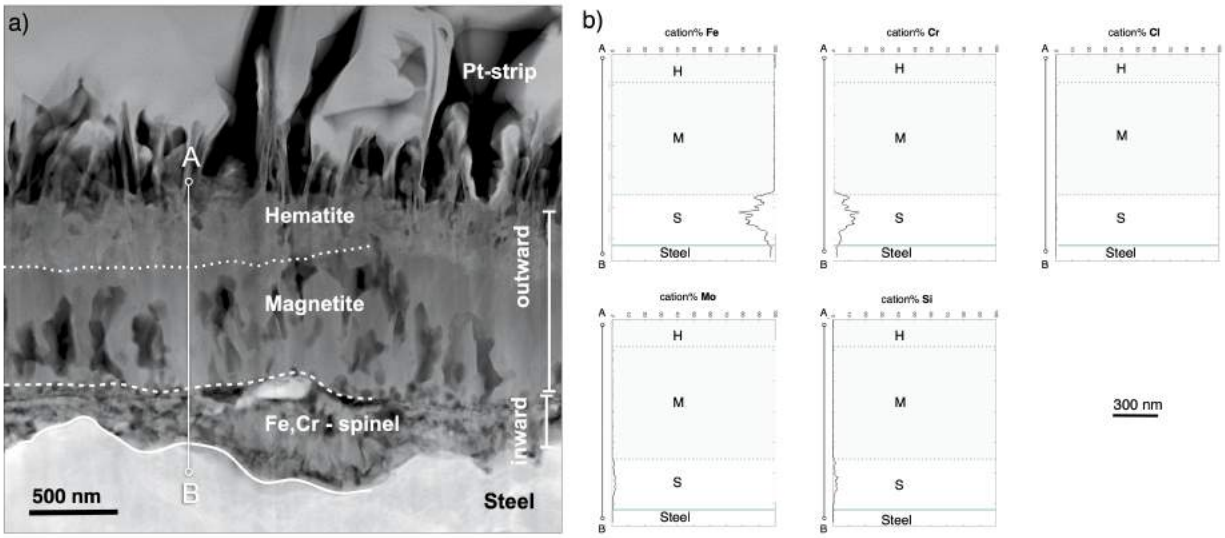

Figure 5.16: HAADF-STEM image and STEM/EDX analysis of the oxide scale formed on Fe-2.25Cr-1Mo steel exposed for 24 hours in the presence of HCl(s) (5% O_2 + 20% H_2O + 74.95% N_2, at 400 °C). The HAADF-STEM image marks the position of the STEM/EDX line-scans shown in b) (see marking A-B). The Cr line-scan indicate the original metal surface and separates the outward- and inward-growing scales. No signal of chlorine is detected by STEM/EDX. The TEM was operated by Dr. Mohammad Sattari.

Influence of HCl(g) and KCl(s)

Figure 5.17 shows that the base-oxide scale formed, in-between the deposited KCl particles, after 24 hours is approximately three times thicker than the oxide scale formed in the presence of HCl(g) only. The oxide scale is well-adherent and attached to the alloy substrate. The amount of inward-growing scale is increased compared to the reference exposure and the exposures that contain only HCl(g) or KCl(s). Thus, the inward diffusion of anions is enhanced to a greater extent in the presence of both KCl(s)+HCl(g).

The STEM/EDX analysis (see Figure 5.17b) shows that all the alloying elements remain in the inward-growing spinel. and that trace amounts of chlorine are present at the scale/metal interface. However, the low concentration and the porosity of this region makes the exact quantification of light elements, such as chlorine, difficult. Further studies, using techniques with lower detection limit and better spatial resolution, are needed to quantify the trace amounts of chlorine and understand how it may influence the corrosion propagation of the secondary corrosion protection.

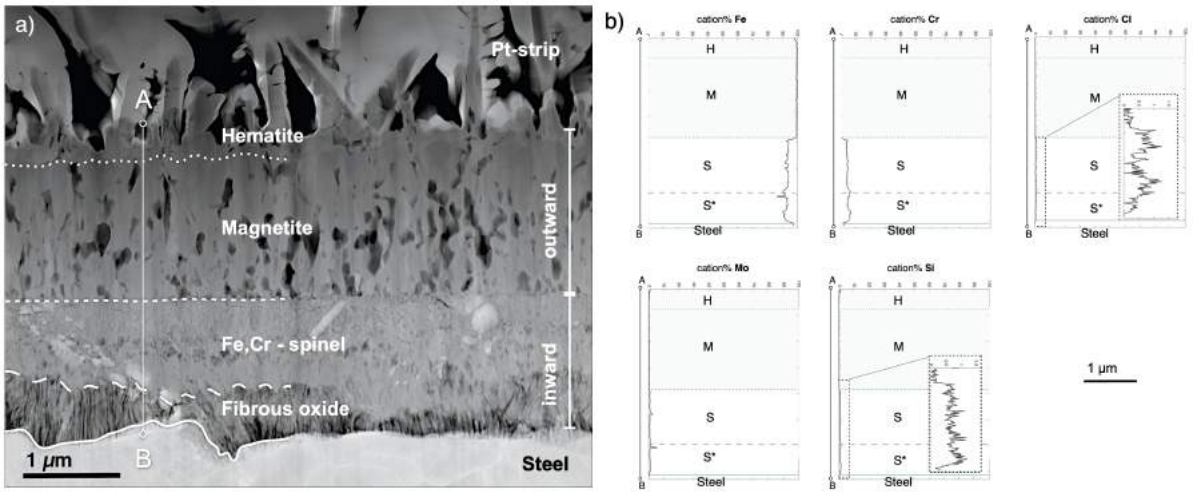

Figure 5.17: HAADF-STEM image and STEM/EDX analysis of the oxide scale formed on Fe-2.25Cr-1Mo steel exposed for 24 hours in the presence of KCl(s) + 500 vppm HCl(g) (5% O_2 + 20%H_2O + 74.95% N_2, at 400 °C). The HAADF-STEM image (a) marks the position of the STEM/EDX line-scans shown in b) (see marking A-B). The STEM/EDX analysis shows that trace amounts of chlorine are detected in at the scale/metal interface. The TEM was operated by Dr. Mohammad Sattari.

Influence of KCl(s)

The oxide scale formed in the presence of KCl(s)-only is shown in Figure 5.18. The oxide scale contains cracks and lateral delamination in contrast to the well-adherent oxide scale formed in the presence of both HCl(g) and KCl(s). The microstructural investigation reveals that a similar multi-layered oxide scale form both above and below the delamination (see Figure 5.18). Both these sub-scales (upper and lower) are similar to the oxide scale formed in the reference exposure, although with different relative amounts of inward- and outward-growing scales. The amount of inward-growing scale is increased compared to

the reference exposure in both the upper (30%) and lower (45%) sub-scales (see Table 5.8. Thus, the amount of inward diffusion of anions is enhanced in the presence of KCl(s).

The STEM/EDX analysis confirms the two sub-scales based on the distribution of alloying elements (see Cr line-scan in Figure 5.18b) and reveals trace amounts (<1 at%) of chlorine at the scale/metal interface and potassium (<1.5 at%) in the top part of the upper sub-scale. The respective levels of chlorine and potassium are low and cannot be quantified with certainty using STEM/EDX. Therefore, the oxide scale should be further studied using a technique with lower detection limit. It should be noted, that the well-adherent oxide scale formed in the presence of both HCl(g) and KCl(s) did not contain any detectable amounts of potassium. Thus, this may imply that potassium in the oxide scale, could influence the mechanical integrity of the multi-layered, Fe-rich oxide scales formed as the secondary corrosion protection at 400 °C.

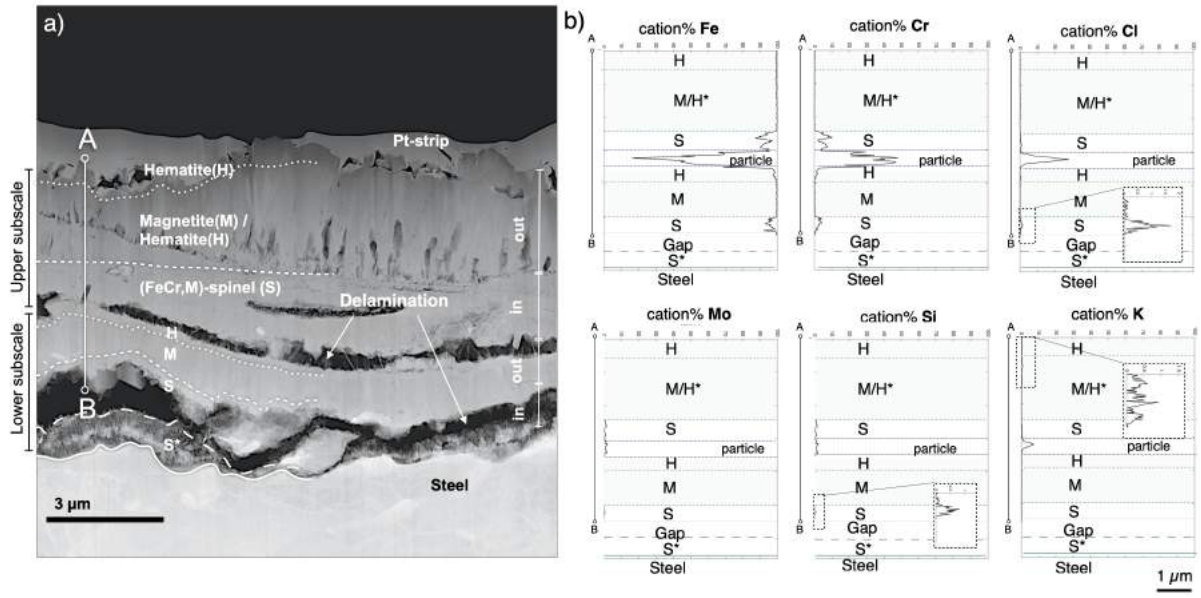

Figure 5.18: HAADF-STEM image and STEM/EDX analysis of the oxide scale formed on Fe2.25Cr1Mo steel exposed for 24 hours in the presence of KCl(s) (5% O_2 + 20%H_2O + 75% N_2, at 400 °C). The Cr line-scan (see marking A-B) shows the presence of two sub-scales. Trace amounts of potassium(K) and chlorine(Cl) are detected in the top part of the upper sub-scale (K) and at the scale/metal interface (Cl). The TEM was operated by Dr. Mohammad Sattari.

To summarise, the microstructural investigation strongly indicate that the oxide microstructure is altered as the corrosive environment is changed. The presence of KCl(s)-only induce cracks and delamination of the oxide scale, indicating that certain corrosive environments may have detrimental effects on the mechanical integrity of the Fe-rich oxide scale. With a lost integrity of the oxide scale, the growth rate and protective properties of the oxide itself becomes irrelevant, since the alloy becomes directly exposed to the corrosive environment if the oxide is lost. Thus, it is of high concern to further study the mechanisms behind the lost integrity of the oxide scale in the presence of e.g KCl(s) and how to suppress this process.

6

Summary & Outlook

This work implements the concept of primary and secondary corrosion regimes before and after breakaway corrosion. The primary corrosion protection is defined as the slow-growing Cr/Al-rich M_2O_3 oxide scale formed on stainless steels and FeCrAl alloys in mildly corrosive environments, while the secondary corrosion protection entails the formation of a faster-growing, multi-layered, Fe-rich oxide scale formed after breakaway corrosion at intermediately high temperatures.

The results show that the secondary corrosion protection of all the exposed FeCr(Ni/Al) model alloys exhibit similar microstructural features. It is suggested that the secondary corrosion protection is predominantly diffusion-controlled, as the primary corrosion protection, at intermediately high temperatures (e.g. 600 °C). Thus, it should be possible to develop lifetime predictive tools for the corrosion both before and after breakaway using diffusion based modelling tools such as e.g. DICTRA [38, 39].

Furthermore, it is shown that the growth rate of the secondary corrosion protection may be influenced by the alloy composition, e.g. by adding Ni or a combination of Al/Cr. The reduced growth rated is not directly connected to how well the primary corrosion protection withstands the exposure environment (i.e. the incubation time to breakaway). Thus, these findings indicate that research on the secondary corrosion protection has a large potential to improve the selection and development of alloys for use in corrosive environments, such as biomass- and waste-fired boilers.

The present work mainly investigates how the oxide microstructures and oxidation properties of the secondary corrosion protection are influenced by altered alloy composition. However, the capacities of the secondary corrosion protections to withstand other corrosive species needs to be studied further. The influences of other corrosive species were studied briefly in this work in terms of oxide scales formed on a low-alloyed steel at 400 °C. The results show that the oxide scale microstructure is strongly influenced as the corrosive species change, e.g. through inducing cracks and delamination of the scale. Thus, in order to truly evaluate the corrosion resistance of stainless steels and FeCrAl alloys for use in harshly corrosive environments, it is suggested to conduct further studies on the secondary corrosion protection in the presence of other corrosive species.

Bibliography

[1] P. Kofstad, *High Temperature corrosion.* London/New York: Elsevier Applied Science, 1988.

[2] N. Birks, G. H. Meier, and F. S. Pettit, *Introduction to the high-temperature oxidation of metals.* Cambridge University Press, 2006.

[3] D. J. Young, *High Temperature Oxidation and Corrosion of Metals (Second Edition).* Elsevier, 2016.

[4] G. C. Wood and D. P. Whittle, "The mechanism of breakthrough of protective chromium oxide scales on Fe-Cr alloys," *Corrosion science*, vol. 7, no. 11, 1967.

[5] F. Stott, G. Wood, and J. Stringer, "The influence of alloying elements on the development and maintenance of protective scales," *Oxidation of metals*, vol. 44, pp. 113–145, 1995.

[6] H. Asteman, J. Svensson, M. Norell, and L. Johansson, "Influence of Water Vapor and Flow Rate on the High-Temperature Oxidation of 304L ; Effect of Chromium Oxide Hydroxide Evaporation," *Oxidation of Metals*, vol. 54, no. 1-2, pp. 11–26, 2000.

[7] H. Asteman, K. Segerdahl, J. E. Svensson, and L. G. Johansson, "The influence of water vapor on the corrosion of chromia-forming steels," *Materials Science Forum*, vol. 369-372, no. I, pp. 277–286, 2001.

[8] S. R. J. Saunders, M. Monteiro, and F. Rizzo, "The oxidation behaviour of metals and alloys at high temperatures in atmospheres containing water vapour : A review," *Progress in Materials Science*, vol. 53, pp. 775–837, 2008.

[9] L. Liu, Z.-G. Yang, M. Zhang, K. Kawamura, and T. Maryama, "Effect of water vapour on the oxidation of Fe-13Cr-5Ni martensitic alloy at 973 K," *Corrosion science*, vol. 60, pp. 90–97, 2012.

[10] J. Ehlers, D. J. Young, E. J. Smaardijk, A. K. Tyagi, H. J. Penkalla, L. Singheiser, and W. J. Quadakkers, "Enhanced oxidation of the 9%Cr steel P91 in water vapour containing environments," *Corrosion Science*, vol. 48, no. 11, pp. 3428–3454, 2006.

[11] T. Jonsson, F. Liu, S. Canovic, H. Asteman, J.-E. Svensson, L.-G. Johansson, and M. Halvarsson, "Influence of H_2O(g) on the Oxide Microstructure of the Stainless Steel 353MA at 900 °C in Oxygen," *Journal of The Electrochemical Society*, vol. 154, no. 11, p. C603, 2007.

[12] B. Pujilaksono, T. Jonsson, H. Heidari, M. Halvarsson, J. E. Svensson, and L. G. Johansson, "Oxidation of binary FeCr alloys (Fe-2.25Cr, Fe-10Cr, Fe-18Cr and Fe-25Cr) in O_2 and in O_2 + H_2O environment at 600 °C," *Oxidation of Metals*, vol. 75, no. 3-4, pp. 183–207, 2011.

[13] T. Jonsson, B. Pujilaksono, H. Heidari, Liu F., J.-E. Svensson, M. Halvarsson, and L.-G. Johansson, "Oxidation of Fe-10Cr in O_2 and in O_2+H_2O environment at 600 °C: A microstructural investigation," *Corrosion science*, vol. 75, pp. 326–336, 2013.

[14] N. K. Othman, J. Zhang, and D. J. Young, "Water vapour effects on Fe-Cr alloy oxidation," *Oxidation of Metals*, vol. 73, no. 1-2, pp. 337–352, 2010.

[15] A. N. Hansson, K. Pantleon, F. B. Grumsen, and M. A. Somers, "Microstructure evolution during steam oxidation of a Nb stabilized austenitic stainless steel," *Oxidation of Metals*, vol. 73, no. 1-2, pp. 289–309, 2010.

[16] E. Essuman, G. H. Meier, J. Zurek, M. Hänsel, L. Singheiser, and W. J. Quadakkers, "Enhanced internal oxidation as trigger for breakaway oxidation of Fe-Cr alloys in gases containing water vapor," *Scripta Materialia*, vol. 57, no. 9, pp. 845–848, 2007.

[17] N. Mu, K. Y. Jung, N. M. Yanar, G. H. Meier, F. S. Pettit, and G. R. Holcomb, "Water vapor effects on the oxidation behavior of Fe-Cr and Ni-Cr alloys in atmospheres relevant to oxy-fuel combustion," *Oxidation of Metals*, vol. 78, no. 3-4, pp. 221–237, 2012.

[18] J. Pettersson, N. Folkeson, L.-G. Johansson, and J.-E. Svensson, "The effects of KCl, K_2SO_4 and K_2CO_3 on the high temperature corrosion of a 304-type austenitic stainless steel," *Oxidation of metals*, vol. 76, pp. 93–109, 2011.

[19] J. Lehmusto, B.-J. Skrifvars, P. Yrjas, and M. Hupa, "Comparison of potassium chloride and potassium carbonate with respect to their tendency to cause high temperature corrosion of stainless 304L steel," *Fuel Processing Technology*, vol. 105, pp. 98–105, 2013.

[20] T. Jonsson, J. Froitzheim, J. Pettersson, J. E. Svensson, L. G. Johansson, and M. Halvarsson, "The influence of KCl on the corrosion of an Austenitic stainless steel (304L) in oxidizing humid conditions at 600 °C: A microstructural study," *Oxidation of Metals*, vol. 72, no. 3-4, pp. 213–239, 2009.

[21] C. Pettersson, L. G. Johansson, and J. E. Svensson, "The Influence of Small Amounts of KCl(s) on the Initial Stages of the Corrosion of Alloy Sanicro 28 at 600 degrees

C," *Oxidation of Metals*, vol. 70, no. 5-6, pp. 241–256, 2008.

[22] A. Col, V. Parry, and C. Pascal, "Oxidation of a Fe–18Cr–8Ni austenitic stainless steel at 850 °C in O_2: Microstructure evolution during breakaway oxidation," *Corrosion Science*, vol. 114, pp. 17–27, 2017.

[23] T. Gheno, D. Monceau, and D. J. Young, "Mechanism of breakaway oxidation of Fe – Cr and Fe – Cr – Ni alloys in dry and wet carbon dioxide," *Corrosion Science*, vol. 64, pp. 222–233, 2012.

[24] F. Liu, J. E. Tang, T. Jonsson, S. Canovic, K. Segerdahl, J. E. Svensson, and M. Halvarsson, "Microstructural investigation of protective and non-protective oxides on 11% chromium steel," *Oxidation of Metals*, vol. 66, no. 5-6, pp. 295–319, 2006.

[25] R. Peraldi and B. A. Pint, "Effect of Cr and Ni Contents on the Oxidation Behavior of Ferritic and Austenitic Model Alloys in Air with Water Vapor," *Oxidation of Metals*, vol. 61, no. 5-6, pp. 463–483, 2004.

[26] T. Jonsson, S. Karlsson, H. Hooshyar, M. Sattari, J. Liske, J.-E. Svensson, and L.-G. Johansson, "Oxidation After Breakdown of the Chromium-Rich Scale on Stainless Steels at High Temperature : Internal Oxidation," *Oxidation of metals*, vol. 85, pp. 509–536, 2016.

[27] T. Jonsson, H. Larsson, S. Karlsson, H. Hooshyar, M. Sattari, J. Liske, J. E. Svensson, and L. G. Johansson, "High-Temperature Oxidation of FeCr(Ni) Alloys: The Behaviour After Breakaway," *Oxidation of Metals*, vol. 87, no. 3-4, pp. 333–341, 2017.

[28] H. P. Nielsen, F. J. Frandsen, K. Dam-Johansen, and L. L. Baxter, "The implications of chlorine-associated corrosion on the operation of biomass-fired boilers," *Progress in Energy and Combustion Science 26*, pp. 283–298, 2000.

[29] M. Spiegel, A. Zahs, and H. J. Grabke, "Fundamental aspects of chlorine induced corrosion in power plants," *Materials at High Temperatures*, vol. 20, no. 2, pp. 153–159, 2003.

[30] M. Montgomery, A. Karlsson, and O. H. Larsen, "Field test corrosion experiments in Denmark with biomass fuels. Part 1: Straw-firing," *Materials and Corrosion*, vol. 53, no. 2, pp. 121–131, 2002.

[31] F. J. Frandsen, "Utilizing biomass and waste for power production - A decade of contributing to the understanding, interpretation and analysis of deposits and corrosion products," *Fuel*, vol. 84, no. 10, pp. 1277–1294, 2005.

[32] P. Henderson, P. Szakalos, R. Pettersson, C. Andersson, and J. Hogberg, "Reducing superheater corrosion in wood-fired boilers," *Materials and Corrosion*, vol. 57, no. 2,

pp. 128–134, 2006.

[33] A. Syed, N. Simms, and J. Oakey, "Fireside corrosion of superheaters: Effects of air and oxy-firing of coal and biomass," *Fuel 101*, pp. 62–73, 2012.

[34] L. Paz, T. Jonsson, and J. Liske, "Testing of new materials to combat superheater corrosion in a waste fired CFB boiler," in *23rd International conference on Fluidized Bed Conversion*, 2018.

[35] S. C. Okoro, M. Montgomery, F. J. Frandsen, and K. Pantleon, "Influence of Preoxidation on High-Temperature Corrosion of a FeCrAl Alloy Under Conditions Relevant to Biomass Firing," *Oxidation of Metals*, vol. 89, no. 1-2, pp. 99–122, 2018.

[36] J. Eklund, M. D. Paz, B. Jönsson, J. Liske, J. E. Svensson, and T. Jonsson, "Field exposure of FeCrAl model alloys in a waste-fired boiler at 600 °C: The influence of Cr and Si on the corrosion behaviour," *Materials and Corrosion*, vol. 70, no. 8, pp. 1476–1485, 2019.

[37] J. Eklund, B. Jönsson, A. Persdotter, J. Liske, J. Svensson, and T. Jonsson, "The influence of silicon on the corrosion properties of FeCrAl model alloys in oxidizing environments at 600 °C," *Corrosion Science*, vol. 144, pp. 266–276, 2018.

[38] J.-O. Andersson, T. Helander, L. Höglund, P. Shi, and B. Sundman, "THERMO-CALC & DICTRA, Computational Tools For Materials Science," *Calphad*, vol. 26, no. 2, pp. 273–312, 2002.

[39] H. Larsson, T. Jonsson, R. Naraghi, Y. Gong, R. C. Reed, and J. Ågren, "Oxidation of iron at 600 °C – experiments and simulations," *Materials and corrosion*, vol. 68:2, pp. 133–142, 2017.

[40] I. Kaur and W. Gust, *Fundamentals of grain and interface boundary diffusion*. Stuttgart: Ziegler press, 1989.

[41] J. Topfer, S. Aggarwal, and R. Dieckmann, "Point defects and cation tracer diffusion in $(Cr_x,Fe_{1-x})_{3-\delta}O_4$ spinels," *Solid State Ionics*, vol. 81, no. 2738, pp. 251–266, 1995.

[42] J. A. V. Orman and K. L. Crispin, "Diffusion in Oxides," *Reviews in Mineralogy and Geochemistry*, vol. 72, pp. 757–825, 2010.

[43] R. Dieckmann, M. R. Hilton, and T. O. Mason, "Defects and Cation Diffusion in Magnetite (Viii): Migration Enthalpies for Iron and Impurity Cations." *Berichte der Bunsengesellschaft/Physical Chemistry Chemical Physics*, vol. 91, no. 1, pp. 59–66, 1987.

[44] V. Tammann, "Uber anlauffarben von metallen," *Z. Anorg. Allg. Chem.*, vol. 111, 1920.

[45] C. Wagner, "Beitrag zur theorie des anlaufvorgangs," *Zeitschrift für physicalische chemie*, vol. 21, no. 1, pp. 25–41, 1933.

[46] F. Stott, "The oxidation of alumina-forming alloys," in *High Temperature Corrosion and Protection of Materials 4*, ser. Materials Science Forum, vol. 251. Trans Tech Publications Ltd, 10 1997, pp. 19–32.

[47] H. Josefsson, F. Liu, J. Svensson, M. Halvarsson, and L. Johansson, "Oxidation of FeCrAl alloys at 500-900 °C in dry O_2," *Materials and Corrosion*, vol. 56, no. 11, pp. 801–805, 2005.

[48] R. Y. Chen and W. Y. D. Yuen, "Review of the High-Temperature Oxidation of Iron and Carbon Steels in Air or Oxygen," *Oxidation of Metals*, vol. 59, no. 1, pp. 433–468, 2003.

[49] R. Kornell and U. Schwertmann, *The iron oxides - Structure, Properties, Reactions, Occurences and Uses*. Wiley-VCH Verlag GmbH & Co. KGaA, 2003.

[50] G. C. Wood, "High-temperature oxidation of alloys," *Oxidation of Metals*, vol. 2, no. 1, pp. 11–57, 1970.

[51] W. Bragg, "The structure of the spinel group of crystals ," *The London, Edinburgh, and Dublin Philosophical Magazine and Journal of Science*, vol. 30, no. 176, pp. 305–315, 1915.

[52] A. Khanna, *Introduction to High Temperature oxidation and corrosion*. ASM International, 2002.

[53] M. G. Hobby, "The Role of Nickel in the High-Temperature Oxidation of Fe-Cr-Ni Alloys in Oxygen," *Oxidation of Metals*, vol. 1, no. 1, pp. 23–54, 1969.

[54] R. F. A. Pettersson, J. Enecker, and L. Liu, "Role of nickel in the oxidation of Fe-Cr-Ni alloys in air-water vapour atmospheres," *Materials at High Temperatures*, vol. 22, no. 3-4, pp. 269–281, 2005.

[55] M. J. McNallan, W. W. Liang, S. H. Kim, and C. T. Kang, "Accelleration of the High Temperature Oxidation of Metals by Chlorine," *High Temperature Corrosion, NACE*, pp. 316–321, 1983.

[56] J. Pettersson, H. Asteman, J. E. Svensson, and L. G. Johansson, "KCl induced corrosion of a 304-type austenitic stainless steel at 600 degrees C; The role of potassium," *Oxidation of Metals*, vol. 64, no. 1-2, pp. 23–41, 2005.

[57] S. Karlsson, J. Liske, L.-G. Johansson, and J.-E. Svensson, "Alkali induced high temperature corrosion of stainless steel: the influence of NaCl, KCl and $CaCl_2$," *Oxidation of metals*, vol. 78, pp. 83–172, 2012.

[58] N. Israelsson, K. A. Unocic, K. Hellström, T. Jonsson, M. Norell, J. E. Svensson, and L. G. Johansson, "A Microstructural and Kinetic Investigation of the KCl-Induced Corrosion of an FeCrAl Alloy at 600 °C," *Oxidation of Metals*, vol. 84, no. 1-2, pp. 105–127, 2015.

[59] N. Israelsson, K. Unocic, K. Hellström, J.-E. Svensson, and L. G. Johansson, "Cyclic Corrosion and Chlorination of an FeCrAl Alloy in the Presence of KCl," *Oxidation of Metals*, vol. 84, no. 1-2, p. 269–290, 2015.

[60] B. B. Ebbinghaus, "Thermodynamics of gas phase chromium species: the chromium chlorides, oxychlorides, fluorides, oxyfluorides, hydroxides, oxyhydroxides, mixed oxyfluorochlorohydroxides, and volatility calculations in waste incineration processes," *Combustion and Flame*, vol. 93, pp. 119–137, 1993.

[61] E. J. Opila, D. L. Myers, N. S. Jacobson, I. M. Nielsen, D. F. Johnson, J. K. Olminsky, and M. D. Allendor, "Theoretical and experimental investigation of the thermochemistry of $CrO_2(OH)_2$(g)," *Journal of Physical Chemistry A*, vol. 111, no. 10, pp. 1971–1980, 2007.

[62] S. Reyntjens and R. Puers, "A review of focused ion beam applications in microsystem technology," *Journal of micromechanics and microengineering 11*, p. 287–300, 2001.

[63] J.Goldstein, D. Newbury, D. Joy, C. Lyman, P. Echlin, E. Lifshin, L. Sawyer, and J. Michael, "Scanning Electron Microscopy and X-ray Microanalysis," *(Third edition)*, 2007.

[64] D. B. Williams and C. B. Carter, *Transmission electron microscopy, A textbook for materials science.* New York: Springer Science + Business Media, 2009.

[65] E. by Stephen J. Pennycook and P. Nellist, *Scanning transmission electron microscopy, Imaging and analysis.* New York: Springer Science + Business Media, 2011.

[66] J. Orloff, M. Utlaut, and L. Swanson, *High Resolution Focused Ion Beams: FIB and its Applications.* New York: Kluwer academic/Plenum publishers, 2003.

[67] D. C. Cox, "Introduction to Focused Ion Beam Nanometrology," *Morgan and Claypool Publishers*, 2015.

[68] B. D. Cullity, *Elements of X-ray diffraction.* Pearson Education, 2014.

[69] R. A. Schwarzer, D. P. Field, B. L. Adams, M. Kumar, and A. J. Schwartz, *Present State of Electron Backscatter Diffraction and Prospective Developments.* Boston, MA: Springer US, 2009, pp. 1–20.

[70] S. Bigdeli, L. Kjellqvist, R. Naraghi, L. Höglund, H. Larsson, and T. Jonsson, "Strate-

gies for high-temperature corrosion simulations of Fe-based alloys using Calphad approach - Part I," unpublished.

[71] N. Folkeson, T. Jonsson, M. Halvarsson, L. G. Johansson, and J. E. Svensson, "The influence of small amounts of KCl(s) on the high temperature corrosion of a Fe-2.25Cr-1Mo steel at 400 and 500 °C," *Materials and Corrosion*, vol. 62, no. 7, pp. 606–615, 2011.

[72] D. Bramhoff, H. J. Grabke, E. Reese, and H. P. Schmidt, "Einfluß von HCl und Cl_2 auf die Hochtemperaturkorrosion des 2 1/4 Cr 1 Mo-Stahls in Atmosphären mit hohen Sauerstoffdrücken," *Materials and Corrosion*, vol. 41, no. 6, pp. 303–307, 1990.

[73] E. Reese and H. J. Grabke, "Einflun von Chloriden auf die Oxidation," *Werkstoffe und Korrosion*, vol. 43, pp. 547–557, 1992.

[74] H. J. Grabke, E. Reese, and M. Spiegel, "The Effects of Chlorides, Hydrogen-Chloride, and Sulfur-Dioxide in the Oxidation of Steels Below Deposits," *Corrosion Science*, vol. 37, no. 7, pp. 1023–1043, 1995.

[75] F. Wang and Y. Shu, "Influence of Cr content on the corrosion of Fe-Cr alloys: The synergistic effect of NaCl and water vapor," *Oxidation of Metals*, vol. 59, no. 3-4, pp. 201–214, 2003.

[76] Y. S. Li, Y. Niu, and W. T. Wu, "Accelerated corrosion of pure Fe, Ni, Cr and several Fe-based alloys induced by $ZnCl_2$-KCl at 450 °C in oxidizing environment," *Materials Science and Engineering*, vol. A345, pp. 64–71, 2003.

[77] M. A. Uusitalo, P. M. J. Vuoristo, and T. A. Mantyla, "High temperature corrosion of coatings and boiler steels in oxidizing chlorine-containing atmosphere," *Materials Science and Engineering a-Structural Materials Properties Microstructure and Processing*, vol. 346, no. 1-2, pp. 168–177, 2003.

[78] S. Środa, S. Tuurna, K. Penttilä, and L. Heikinheimo, "High Temperature Oxidation Behaviour of Boiler Steels under Simulated Combustion Gases," *Materials Science Forum*, vol. 461-464, pp. 981–988, 2004.

[79] M. A. Uusitalo, P. M. J. Vuoristo, and T. A. Mantyla, "High temperature corrosion of coatings and boiler steels below chlorine-containing salt deposits," *Corrosion Science*, vol. 46, no. 6, pp. 1311–1331, 2004.

[80] S. Sroda and S. Tuurna, "Laboratory scale tests on corrosion behavior of boiler materials in simulated combustion atmospheres (EU Project - OPTICORR)," *Materials and Corrosion*, vol. 57, no. 3, pp. 244–251, 2006.

[81] T. Jonsson, N. Folkeson, J.-E. Svensson, L.-G. Johansson, and M. Halvarsson, "An ESEM in situ investigation of initial stages of the KCl induced high temperature

corrosion of a Fe–2.25Cr–1Mo steel at 400 °C," *Corrosion science*, vol. 53, pp. 2233–2246, 2011.

[82] A. M. Olivas Ogaz, J. Eklund, A. Persdotter, M. Sattari, J. Liske, J.-E. Svensson, and T. Jonsson, "The Influence of Oxide-Scale Microstructure on KCl(s)-Induced Corrosion of Low-Alloyed Steel at 400 °C," *Oxidation of Metals*, vol. 91, no. 3-4, pp. 291–310, 2019.

[83] E. Larsson, J. Liske, A. Persdotter, T. Jonsson, J. E. Svensson, and L. G. Johansson, "The Influence of KCl and HCl on the High-Temperature Oxidation of a Fe-2.25Cr-1Mo Steel at 400 °C," *Oxidation of Metals*, vol. 93, no. 1-2, pp. 29–52, 2020.

[84] A. Zahs, M. Spiegel, and H. J. Grabke, "The influence of alloying elements on the chlorine-induced high temperature corrosion of Fe-Cr alloys in oxidizing atmospheres," *Materials and Corrosion*, vol. 50, no. 10, pp. 561–578, 1999.

[85] N. Folkeson, L. G. Johansson, and J. E. Svensson, "Initial stages of the HCl-induced high-temperature corrosion of alloy 310," *Journal of the Electrochemical Society*, vol. 154, no. 9, pp. C515–C521, 2007.

[86] J. Pettersson, J.-E. Svensson, and L.-G. Johansson, "Alkali induced corrosion of 304-type austenitic stainless steel at 600 °C; comparison between KCl, K_2CO_3 and K_2SO_4," *Materials Science Forum*, vol. 595-598 PA, pp. 367–375, 2008.

[87] H. T. Ma, C. H. Zhou, and L. Wang, "High temperature corrosion of pure Fe, Cr and Fe-Cr binary alloys in O_2 containing trace KCl vapour at 750 °C," *Corrosion Science*, vol. 51, no. 8, pp. 1861–1867, 2009.

[88] C. Proff, T. Jonsson, C. Pettersson, J. E. Svensson, L. G. Johansson, and M. Halvarsson, "Microstructural investigation of the KCl-induced corrosion of the austenitic alloy Sanicro 28 (35Fe27Cr31Ni) at 600 °C," *Materials at High Temperatures*, vol. 26, no. 2, pp. 113–125, 2009.

[89] J. Sui, J. Lehmusto, M. Bergelin, and H. Mikko, "The Effects of KCl, NaCl and K_2CO_3 on the High-Temperature Oxidation Onset of Sanicro 28 Steel," *Oxidation of metals*, vol. 85, pp. 565–598, 2016.

[90] N. Bertrand, C. Desgranges, D. Gauvain, D. Monceau, and D. Poquillon, "Low Temperature Oxidation of Pure Iron : Growth kinetics and scale Morphologies," *Materials Science Forum*, vol. 461-464, pp. 591–598, 2004.

[91] B. Pujilaksono, T. Jonsson, M. Halvarsson, J. E. Svensson, and L. G. Johansson, "Oxidation of iron at 400-600 °C in dry and wet O_2," *Corrosion Science*, vol. 52, no. 5, pp. 1560–1569, 2010.